

Optical Amplification and Lasing by Stimulated Raman Scattering in Silicon Waveguides

Ansheng Liu, Haisheng Rong, Richard Jones, Oded Cohen, Dani Hak, and Mario Paniccia, *Senior Member, IEEE*

Invited Paper

Abstract—Achieving light amplification and lasing in silicon is one of most challenging goals in silicon-based optoelectronics. As a nonlinear optical effect, stimulated Raman scattering (SRS) provides a means to generate optical gain in silicon. Recent results of a nonlinear optics approach to optical amplification and lasing in silicon at the Photonics Technology Laboratory of Intel Corporation are reviewed. This paper starts with the description of the underlying physics related to the Raman scattering in silicon and experimental results of SRS in silicon waveguides. Then, it is shown that nonlinear optical absorption associated with the two-photon absorption (TPA)-induced free carrier absorption (FCA) is a dominant loss mechanism limiting optical gain in a silicon waveguide in addition to the linear optical scattering loss due to the waveguide sidewall roughness. The design and fabrication of a low-loss silicon waveguide containing a p-i-n diode to reduce the nonlinear optical loss are described. It is demonstrated that the free carrier density inside the waveguide can be reduced significantly with a reverse bias of the p-i-n diode. As a result, net optical gain in a silicon waveguide is achieved. The design, fabrication, and characterization of a Raman silicon laser are also described. Both pulsed and continuous-wave (CW) lasing in silicon are achieved using SRS.

Index Terms—Integrated photonic circuits, planar lightwave circuits, Raman amplifier, Raman laser, Raman scattering, silicon laser, silicon-on-insulator (SOI), silicon photonics, waveguide.

I. INTRODUCTION

MOORE'S law plays an important role in the microelectronics industry, particularly in the microprocessor industry. It suggests that the transistor number in a microprocessor is doubled in every 18 months, enhancing the device performance and lowering the cost. The recent trend of multicore processors will continue to take advantage of Moore's law. Moving to many cores, future microprocessors will require higher data transmission rate for distributed computer systems. As low-cost electric interconnect technology gradually approaches its data transmission capacity limit, optical interconnect is a natural replacement technology for the future because of its inherent enormous bandwidth. Silicon photonics [1], [2] may play an important role in the low-cost optical interconnect technology, as silicon-based optical components

could be manufactured using the existing complementary metal–oxide–semiconductor (CMOS) silicon fabrication techniques. To “siliconize” photonics, one needs a silicon-based light source, silicon waveguide, silicon optical modulator, and a silicon-based photodetector. The silicon/silicon dioxide system provides an ideal platform for guiding light with a possible high photonic device density because of the large refractive index contrast. A recent demonstration of a fast silicon modulator [3], [4] suggests that high-frequency modulation in silicon is achievable. SiGe and Ge-on-Si photodetectors are promising for the detection of near-infrared light [5], [6]. So far, the only missing piece of the key building blocks for silicon photonics is the silicon light source.

As single crystal silicon is an indirect band gap semiconductor, it has been traditionally considered impossible to get efficient light emission out of silicon. The primary reason is that silicon has a long (milliseconds) radiative recombination lifetime but a relatively short (nanoseconds) nonradiative lifetime so that the internal quantum efficiency of light emission in silicon is very small ($\sim 10^{-6}$). To try and circumvent this problem, various approaches based on silicon-engineered materials have been attempted. Observation of very efficient visible light emission in porous silicon in the early 1990s [7], [8] boosted the hopes that silicon could be used as a laser active material in the form of nanostructures. Since then, light emission from various silicon nanostructures prepared by a variety of techniques have been extensively investigated [9]–[20]. Although the exact radiative recombination processes involved in these quantum structures are still being debated, the main idea was to confine carriers into tiny silicon nanoclusters (Si-nc) (1–4 nm in size) so that quantum confinement effects began to play a crucial role by changing the physical properties of bulk silicon. As a result, optical gain has been observed in small Si-nc dispersed in a dielectric matrix [16], [20]. During the 1990s, various efforts were also made to develop an efficient and reliable light source using Er^{3+} in silicon [21]–[27]. Room-temperature emission with an external quantum efficiency of 0.1% in a megahertz-modulated Er^{3+} -based light-emitting device (LED) has been demonstrated [23]. Using an Er^{3+} -doped Si-nc waveguide, an internal gain of 4 dB/cm was deduced by dividing the waveguide output signal measured with the pump light on by the signal measured with the pump light off [26]. In addition, light emission from dislocation-engineered silicon has been

Manuscript received May 9, 2005; revised October 20, 2005.

A. Liu, H. Rong, R. Jones, and M. Paniccia are with Intel Corporation, Santa Clara, CA 95054 USA.

O. Cohen and D. Hak are with Intel Corporation, Jerusalem 91031, Israel.
Digital Object Identifier 10.1109/JLT.2005.863322

investigated [28]–[30]. Light emission in Si/SiGe superlattices was also studied [31].

As is well known, Raman scattering, which is a nonlinear optics effect, provides an alternative way to generate optical gain [32]. Currently, commercially available fiber Raman amplifiers and lasers are based on the Raman effect. Raman scattering in bulk silicon was studied as early as 1965 [33]. Using a helium–neon laser with an output wavelength of $0.6328 \mu\text{m}$, backward Raman scattering from silicon was measured, and it was found that the Raman scattering efficiency in silicon was 35 times larger than that for diamond [33]. In 1970 [34], more detailed Raman experiment using a YAG:Nd laser having a wavelength of $1.064 \mu\text{m}$ was performed. Both spontaneous and stimulated Raman scattering (SRS) efficiency was characterized experimentally [34]. The observed Raman frequency-downward shift of 15.6 THz corresponds to optical phonon energy of silicon at the center of the Brillouin zone [35], [36]. These experiments showed that silicon has a relatively strong Raman scattering efficiency (four orders of magnitude higher than that for silica) [32], [37], [38]. As silicon is transparent in $1.3\text{--}1.6 \mu\text{m}$ (optical communication band), Raman scattering in silicon waveguides in such a wavelength range has attracted a great deal of interest in the past couple of years [37]–[49]. Both spontaneous scattering [37], [40] and SRS [38], [41] in a silicon waveguide in silicon-on-insulator (SOI) have been measured. Several groups have reported efficient Raman amplification in silicon waveguides with various waveguide dimensions. Pulsed [42]–[45] and continuous-wave (CW) [47] net optical gain was demonstrated. Pulsed lasing has been achieved using a ring cavity formed by an 8-m-long optical fiber and silicon as the gain medium via SRS [46]. In particular, an all-silicon Raman laser has been demonstrated using centimeter-size silicon waveguide [48], [49].

In this paper, we review research results on the Raman scattering in silicon waveguide at Intel Corporation. We show that nonlinear optical absorption associated with the two-photon absorption (TPA)-induced free carrier absorption (FCA) is a dominant loss mechanism limiting optical gain in a silicon waveguide in addition to the linear optical scattering loss due to the waveguide sidewall roughness. We describe the design and fabrication of a low-loss silicon waveguide containing a p-i-n diode. We demonstrate both theoretically and experimentally that the free carrier density inside the waveguide can be reduced significantly with a reverse bias of the p-i-n diode. As a result, we achieve net optical gain in a silicon waveguide. We also describe the design, fabrication, and characterization of a Raman silicon laser. We achieve both pulsed and CW lasing in silicon using SRS.

The paper is organized into six sections. In Section II, we overview the Raman scattering in a silicon waveguide. The key issue to realize net optical gain in silicon is also discussed. In Section III, we review our approach to net gain in silicon. We describe the design of a p-i-n diode waveguide, modeling of the carrier density in the p-i-n diode waveguide, and experiment on the nonlinear optical loss reduction of the silicon waveguide by a reverse bias of the p-i-n diode. Section IV describes the net optical gain characterization of a silicon waveguide. In Section V, we present results on the Raman silicon laser. Both

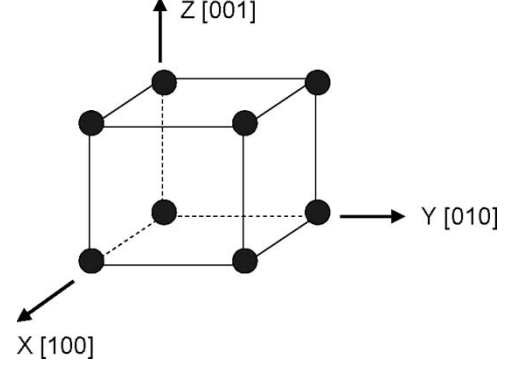


Fig. 1. Crystal axes in a cubic unit cell used in the description of the Raman scattering tensor in silicon.

pulsed and CW operations are covered. Finally, we provide a summary in Section VI.

II. RAMAN SCATTERING IN A SILICON WAVEGUIDE

Raman scattering intensity in silicon depends on the directions of the polarization vectors of the incident (pump) light and scattered (Stokes) light relative to crystallographic axes. Spontaneous Raman scattering efficiency (S) can be described by [34]

$$S = S_0 \sum_{i=1}^3 [e_p R_i e_s]^2 \quad (1)$$

where e_p and e_s are the unit vectors describing the polarization of pump beam and scattered radiation, respectively. The tensors R_i ($i = 1, 2$, and 3) represent the three degenerate lattice vibrations contribution to the Raman scattering. In the coordinate system of the crystal's primitive (cubic) translation vectors, as shown in Fig. 1, these tensors read as [34]

$$R_1 = \begin{bmatrix} 0 & 1 & 0 \\ 1 & 0 & 0 \\ 0 & 0 & 0 \end{bmatrix} \quad R_2 = \begin{bmatrix} 0 & 0 & 1 \\ 0 & 0 & 0 \\ 1 & 0 & 0 \end{bmatrix} \quad R_3 = \begin{bmatrix} 0 & 0 & 0 \\ 0 & 0 & 1 \\ 0 & 1 & 0 \end{bmatrix}. \quad (2)$$

The quantity S_0 in (1) represents the polarization and crystal-orientation-independent Raman scattering efficiency. Due to the degeneracy of the longitudinal optical (LO) and transverse optical (TO) phonon modes at the Γ -point, forward and backward Raman scattering in silicon has an equal efficiency. When the pump beam is strong enough, SRS occurs. The stimulated Raman gain coefficient (g_r) can be obtained from the spontaneous scattering efficiency and linewidth by [34]

$$g_r = \frac{8\pi^2 c^2}{\hbar \omega_s^3} \frac{S}{n^2 (N_0 + 1) \Delta\omega}. \quad (3)$$

Here, ω_s is the angular frequency of the Stokes emission, c is the light velocity in vacuum, \hbar is Planck constant divided by 2π , n is the refractive index of silicon at the Stokes frequency, N_0 is the Bose factor (0.1 at room temperature), and $\Delta\omega$ is the half-width at half-maximum of the Stokes line in units of angular frequency. As the spontaneous scattering efficiency in silicon

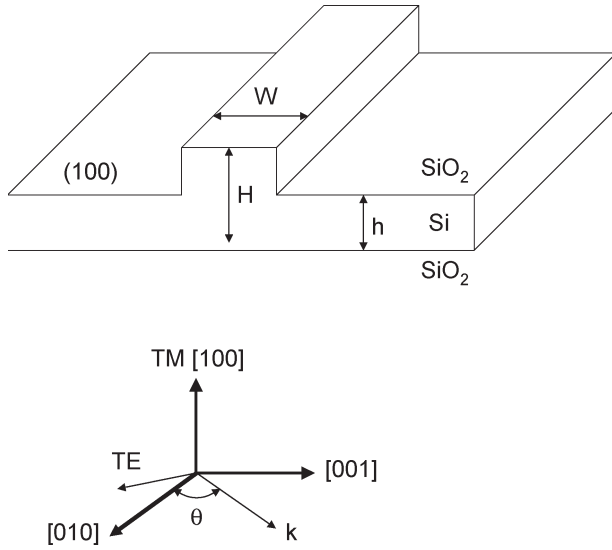


Fig. 2. Schematic of a silicon rib waveguide fabricated on a (100) surface of SOI having rib width of W , rib height of H , and slab height of h . Optical mode propagation direction (\mathbf{k}) and TE and TM mode polarization directions relative to the crystal axes are also displayed.

is pump and Stokes polarization and silicon crystal orientation dependent, we should expect different stimulated Raman gain coefficients with different pump and Stokes radiation polarization and propagation directions. This also provides a means of analyzing the crystallographic orientation by examining the anisotropy of the Raman intensity [50].

In order to obtain a large optical gain due to SRS in silicon, it is preferable to use a silicon waveguide configuration, since the optical interaction length can be increased by increasing the waveguide length. Assuming the optical phonon properties of the silicon waveguide is the same as in bulk silicon, one can use the same formalism outlined above to describe the Raman gain coefficient due to SRS in a silicon waveguide. As high-quality silicon-on-insulator (SOI) wafers are currently commercially available, silicon waveguide in SOI can be readily created by standard CMOS fabrication technique. Fig. 2 shows schematically a silicon waveguide having a rib width W , rib height H , and a slab height h . With a proper choice of these waveguide dimensions [1], [51], [52], one can obtain a single-mode waveguide that supports one transverse electric (TE) mode and one transverse magnetic (TM) mode. Assuming such a waveguide is fabricated on a (100) surface SOI wafer, which is usually used in experiments, the optical mode propagation direction (\mathbf{k}) is confined in the surface of (100). As both straight and bended SOI waveguides may be used in practical devices, it would be useful to understand the Raman intensity dependence on the waveguide orientation and the light polarizations. For the TM polarization, the pump and Stokes polarization vectors are

$$e_p = [1 \ 0 \ 0] \quad e_s = \begin{bmatrix} 1 \\ 0 \\ 0 \end{bmatrix}. \quad (4)$$

Assuming the waveguide is orientated along a direction with an angle θ from the [010] direction, as shown in Fig. 2, we

find out that the pump and Stokes polarization vectors for TE-polarized light are given by

$$e_p = [0 \ \sin \theta \ -\cos \theta] \quad e_s = \begin{bmatrix} 0 \\ \sin \theta \\ -\cos \theta \end{bmatrix}. \quad (5)$$

Inserting (2), (4), and (5) into (1), we obtain the following Raman scattering efficiency for a (100) surface SOI waveguide:

$$S^{\text{TE-TE}} = 4S_0 \sin^2 \theta \cos^2 \theta \quad (6)$$

$$S^{\text{TE-TM}} = S_0 \quad (7)$$

$$S^{\text{TM-TE}} = S_0 \quad (8)$$

$$S^{\text{TM-TM}} = 0. \quad (9)$$

In (6)–(9), the first superscript in the Raman scattering efficiency describes the pump polarization and the second superscript describes the Stokes polarization. Equation (9) suggests that there is no TM Stokes emission with a TM pump beam. It also appears that TE–TM and TM–TE pump–Stokes polarization combinations lead to the same scattering intensity. For TE–TE polarization combination, however, the scattering efficiency varies between zero ($\theta = 0$ or 90°) and the maximum value S_0 ($\theta = 45^\circ$). In the case of $\theta = 45^\circ$, the waveguide is orientated along the [011] direction.

The UCLA group made a first measurement of spontaneous Raman emission in silicon waveguides on SOI in 2002 and deduced the Raman gain coefficient [37]. In 2003, the same group reported the SRS in a silicon waveguide [38]. In their SRS experiment, a 1.8-cm-long waveguide with an effective core size of $5.4 \mu\text{m}^2$ was used and waveguide loss was $\sim 1.5 \text{ dB/cm}$. Here, the effective core area of the waveguide is defined as [32]

$$A_{\text{eff}} = \frac{\left[\iint |\phi(x, y)|^2 dx dy \right]^2}{\iint |\phi(x, y)|^4 dx dy} \quad (10)$$

where $\phi(x, y)$ is the electric field profile of the optical mode. Using a pump–probe method, a small Raman gain of 0.25 dB (6%) was observed with 1.6-W CW pump power [38]. We should note here that the 0.25-dB gain was obtained by comparing the probe output signal at the Stokes wavelength to that of the Stokes wavelength ($g_r = 0$). Thus, the gain reported in [38] does not represent the net gain of the silicon waveguide, which is defined as the ratio between the output and input powers of the waveguide. As the pump intensity in this experiment was relatively small, the TPA was not considered to have a significant effect on the Raman scattering [38].

For practical optoelectronic applications using SRS in silicon waveguides, significantly higher gain with lower pump power is necessary. As the Raman gain is determined by the pump intensity, using a smaller cross section waveguide would reduce the required pump power to achieve higher gain. To this end, we designed and fabricated a silicon waveguide with a smaller dimension. We performed the SRS measurement using such a small waveguide with a much improved waveguide transmission [41]. The silicon rib waveguide used in our experiment

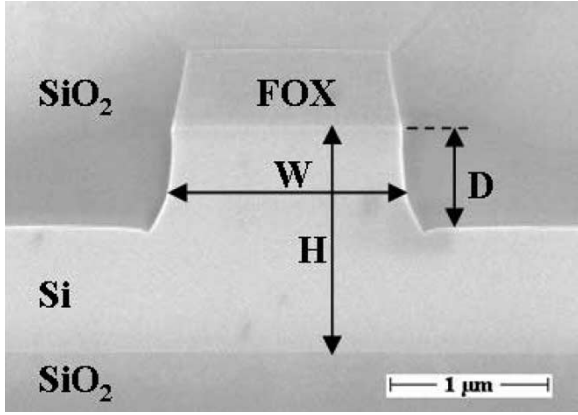


Fig. 3. SEM image of a silicon rib waveguide used for Raman gain and nonlinear optical transmission measurements.

is fabricated on (100) surface of an SOI substrate using standard photolithographic patterning and reactive ion etching techniques. The rib waveguide width is $1.52 \mu\text{m}$, the rib height is $1.45 \mu\text{m}$, and the etch depth is $0.63 \mu\text{m}$. A scanning electron microscope image of the waveguide cross section is shown in Fig. 3. The effective core area of the waveguide is calculated to be $\sim 1.7 \mu\text{m}^2$ using a commercial software Fimmwave [53]. To increase the interaction length but keep the device within a die, the waveguide was formed in an S-shaped curve with a total length of 4.8 cm and a bend radius of $400 \mu\text{m}$. The straight sections of the waveguide are oriented along the [011] direction.

Before performing nonlinear optical measurements, we characterized the linear optical transmission loss of the waveguide. We used Fabry–Pérot (FP) resonance technique to measure the linear optical propagation loss of the waveguide [1]. For this purpose, the waveguide facets were optically polished but uncoated, forming an FP cavity. We measured FP fringes generated using a tunable laser around the wavelength of $1.55 \mu\text{m}$ and modeled the waveguide/air interface reflection coefficient by using a three-dimensional (3-D) FDTD method [54]. The waveguide loss (α) is then obtained by [1]

$$\alpha = -\frac{1}{L} \ln \left(\frac{1}{R} \frac{\sqrt{\zeta} - 1}{\sqrt{\zeta} + 1} \right) \quad (11)$$

where ζ is the ratio of the maximum intensity to minimum intensity of the FP fringe, R is the waveguide facet reflectivity, and L is the waveguide length. Here, we note that the waveguide facet reflectivity R for a small waveguide is polarization dependent and usually quite different from that obtained using a standard normal incidence Fresnel formula with an effective refractive index of the optical mode. This is due to the fact that there is a strong light diffraction effect at the waveguide end because of the high refractive index contrast between silicon and air. With the waveguide geometry in Fig. 3, the calculated facet reflectivity is 33.2% for TE mode and 27.6% for TM mode. Using the measured FP fringe contrast for the 4.8-cm-long silicon waveguide including the double S-bends, we obtained a linear loss of $0.22 \pm 0.05 \text{ dB/cm}$ for both TE and TM modes. The loss uncertainty includes the waveguide-to-waveguide variation and experimental error.

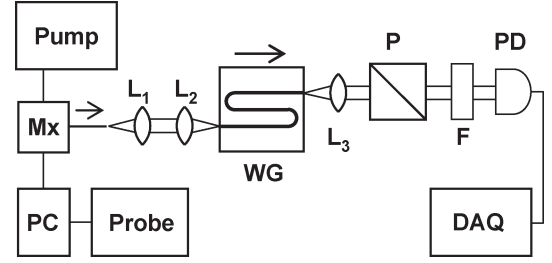


Fig. 4. Schematic pump-probe setup for SRS gain and nonlinear loss measurements. Pump: 1455-nm pump laser; probe: tunable probe laser; Mx: wavelength multiplexer; PC: polarization controller; L_1 , L_2 and L_3 : objective lenses; WG: S-shaped SOI waveguide; P: polarizer; F: optical filter; PD: photodetector; DAQ: data acquisition unit.

In order to minimize the waveguide facet reflection effect on the nonlinear optical measurement, we applied an antireflection (AR) coating to both facets of the waveguide. Using these AR-coated low-loss waveguides, we performed pump-probe and nonlinear optical transmission measurements. Fig. 4 shows a schematic of the experimental setup. The pump and probe lasers are combined with a wavelength multiplexer into a single-mode fiber whose output is coupled into the waveguide under investigation through free space mode-matching optics consisting of a pair of microscope objective lenses mounted on precision alignment stages. The output beam of the waveguide is collimated by another objective lens, and an optical filter is used to separate the pump and probe beams. The probe beam passes through the filter and is detected with a broadband photodetector while the pump beam is blocked by the filter. A polarizer on the output side of the waveguide is used in combination with the polarization controller on the input side to set the polarization of the probe beam. The pump laser is unpolarized. The coupling efficiency into the waveguide is estimated to be $\sim 30\%$ by measuring the input and output power of the waveguide and taking the waveguide loss into account. The power measurements were taken between the objective lenses on the input side and after the collimating lens at the output side.

For the Raman gain measurements, the pump laser is a CW Raman fiber laser operating at 1455 nm, and the probe laser is an external cavity tunable diode laser with a linewidth of $\sim 100 \text{ kHz}$. The probe laser power is 2.6 mW, and its polarization is aligned with the TE mode of the waveguide. To measure the SRS gain, the probe laser is scanned continuously over the Stokes wavelength (Raman gain peak), and the gain profiles at different pump power levels are measured by the photodetector and registered by the data acquisition system.

Fig. 5(a) shows a typical probe output spectrum of a 4.8-cm-long waveguide for a given pump power. As the first-order Raman frequency shift is 15.6 THz (optical phonon frequency) for silicon and the pump wavelength is 1455 nm, the SRS gain peak is expected to be around 1574 nm. We see in Fig. 5(a) that the Raman gain profile is centered at 1574.3 nm, which matches the Raman shift value in the literature [34]–[38]. The gain spectrum shape well approximates a Gaussian function (see the solid curve). Fig. 5(a) also shows that the full-width at half-maximum (FWHM) of the gain profile is $\sim 1 \text{ nm}$ ($\sim 125 \text{ GHz}$). Here, we note that the width of the gain profile is

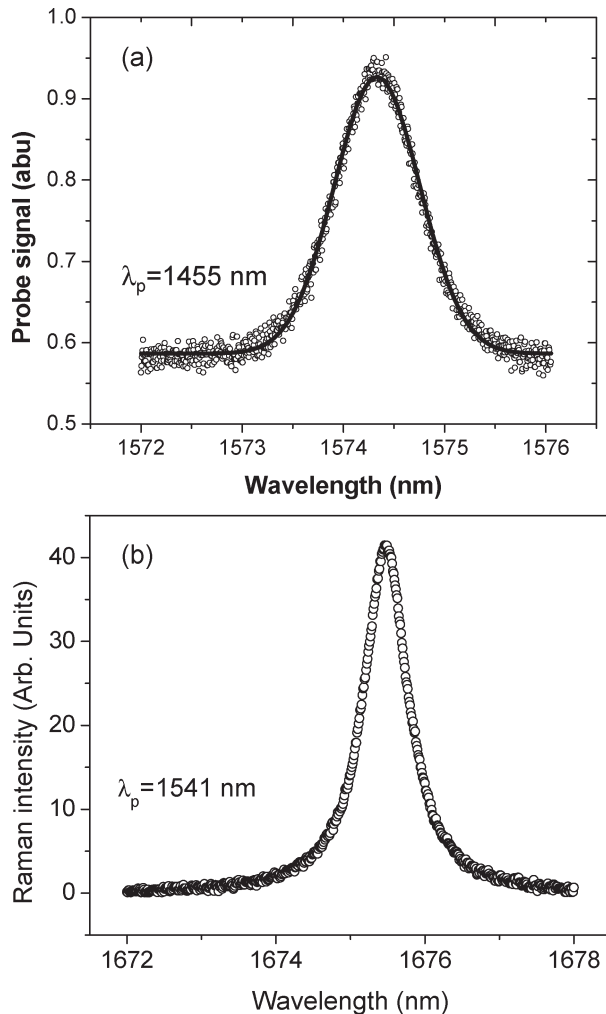


Fig. 5. (a) Raman gain spectrum obtained using a pump laser of 600 mW and a wavelength of 1455 nm. The pump laser linewidth is 76 GHz. A Gaussian curve (solid line) is fitted to the measurement data. (b) Spontaneous Raman emission spectrum obtained using a pump laser of 700 mW and a wavelength of 1541 nm. The pump laser linewidth is < 1 MHz. The spectrum well approximates a Lorentzian function.

basically determined by the width of the Raman gain spectrum and the linewidth of the pump laser. The linewidth of the pump laser used in our experiment slightly depends on its output power (the higher the power, the wider the linewidth). At an output power of 600 mW, it was measured to be 76 GHz. As the pump laser linewidth is less than two times narrower than that of the SRS gain spectrum, we expect that it would contribute significantly to the measured probe spectrum width in Fig. 5(a). To better understand the Raman gain spectrum of our devices, we measured the spontaneous Raman emission spectrum generated by using a much narrower band pump laser (linewidth is < 1 MHz). At a pump power of 700 mW, the Raman intensity as a function of the wavelength obtained using an optical spectrum analyzer with a 0.06-nm resolution is shown in Fig. 5(b). We see in Fig. 5(b) that the Raman spectrum peak is at ~ 1675.5 nm corresponding to the Stokes shift of the pump wavelength of 1541 nm. The FWHM of the spectrum is found to be 87 GHz. This value is about 30% less than reported in the previous publications [38]. We also

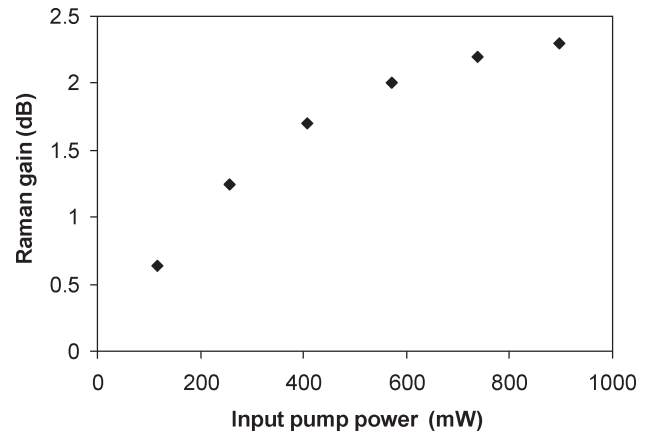


Fig. 6. Measured peak Raman gain as a function of the input pump power. The pump laser wavelength is 1455 nm, and the linewidth is ~ 76 GHz. See the text for the definition of the peak Raman gain.

note in Fig. 5(b) that the spontaneous Raman spectrum well approximates a Lorentzian function. The different spectrum lineshapes in Fig. 5(a) and (b) may be attributed to the different pump laser linewidths and shapes.

Fig. 6 shows the peak Raman gain in the waveguide as a function of the input pump power. The peak gain value is determined by fitting the Raman gain profile for each input pump power with a Gaussian function assuming no Raman gain when the probe laser is detuned far from the peak. Thus, the peak gain describes the relative change in the probe output signals on the Stokes wavelength and off the Stokes wavelength for a given pump power. We see in Fig. 6 that, at an input power of 900 mW (before coupling into the waveguide), a Raman gain of 2.3 dB (70%) was obtained. We also note in Fig. 6 that, although the gain increases with the pump power, it does not grow linearly as would be expected when only the linear optical attenuation of the waveguide is present [32]. This cannot be explained by the pump laser linewidth variation with the output power. In our experiment, we also observed that the probe output signal was always smaller than the input signal, even when we got a 2.3-dB Raman gain, namely, no net gain was obtained even when the linear optical loss of the waveguide is only ~ 1 dB. This suggests that there is additional optical loss in the silicon waveguide induced by the strong pump beam. Such a nonlinear optical loss is clearly a major hurdle to achieve net gain in silicon waveguides.

To obtain a better understanding of the nonlinear behavior of the Raman gain as a function of the pump power as well as the origin of the pump-induced nonlinear optical loss, we measured the pump beam transmission versus input power. Results (with diamond symbols) are shown in Fig. 7. As can be seen, the pump transmission is also clearly nonlinear. One of the possible nonlinear absorption mechanisms in silicon is TPA, since the two-photon energy of the pump beam well exceeds the energy band gap of silicon. The TPA in silicon waveguides in the wavelength range of interest was previously measured with an ultrashort pulse [55], [56]. Using the reported TPA coefficient, the nonlinear absorption seen in Fig. 7 cannot be explained.

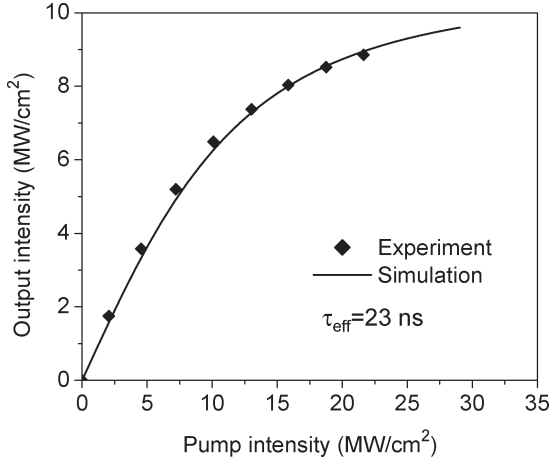


Fig. 7. Measured (symbols) and modeled (solid curve) transmitted optical intensity as a function of the input intensity for a 4.8-cm-long silicon waveguide. An effective carrier lifetime of $\tau_{\text{eff}} = 23$ ns is used in the modeling. See the text for details on other modeling parameters.

In the TPA process, two photons are absorbed simultaneously, and an electron-hole pair is created in the silicon waveguide. Although the pure TPA effect should be small in our experiment according to the ultrafast laser measurement results [55], [56], under CW pump condition, the cumulative free carrier density can reach a significant level because of the finite carrier lifetime in silicon. These free carriers will lead to additional optical absorption, as has been shown in GaAs [57] and InP-InGaAsP [58] waveguides. Taking into account the TPA and TPA-induced FCA (the detailed description of the formalism used in the modeling will be discussed later in this paper), we calculated the transmitted pump power as a function of the pump input power. The result obtained with an effective carrier lifetime of 23 ns is shown by the solid curve in Fig. 7. We see in Fig. 7 that there is a very good agreement between modeling and testing.

To confirm the carrier lifetime obtained by fitting the model to the measured nonlinear transmission, we also performed a pump-probe experiment using a pulsed pump laser operating at 1545 nm with a peak power of ~ 5 W and pulsewidth of 17 ns. The CW probe laser has 4 mW power, and its wavelength is at 1575 nm, where the filter has sufficiently large (60 dB) suppression of the pump pulse. Fig. 8 shows a transient probe signal attenuation due to FCA generated by a short pump pulse. The attenuation indicates an increase of the free carrier density in the waveguide. We can see that the probe signal recovers exponentially as the photo-generated carriers decay. Fitting to the decaying curve gives an effective carrier lifetime of ~ 25 ns, which is in a good agreement with the value (23 ns) obtained from the modeling.

Before closing this section, we would like to mention that the research group at Hong Kong had also independently identified that the TPA-induced FCA was a major hurdle to realize optical amplification using silicon waveguide in the optical communication wavelength band [39], [44]. It is therefore critical to introduce effective measures to reduce the TPA-induced effect. In the following section, we show that it is possible to reduce the TPA-induced free carrier density by embedding a reversely biased p-i-n diode in a silicon waveguide.

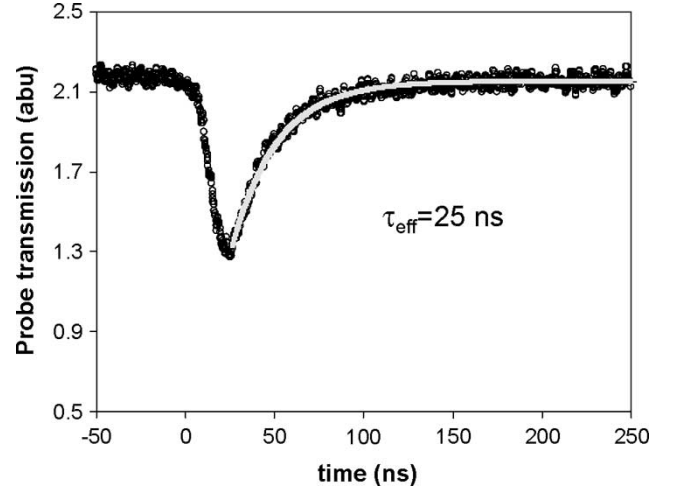


Fig. 8. Time dependence of the transmitted probe signal of a silicon waveguide excited by a pump pulse of pulse width 17 ns. The probe signal decreases as the pump power increases. When the pump pulse walks away, the probe signal recovers because of the carrier density decaying. Fitting to the measurement data with an exponential curve (solid line) gives a decay time constant of 25 ns.

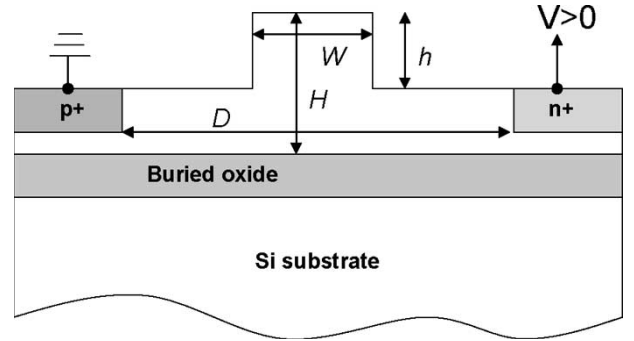


Fig. 9. Schematic of a silicon rib waveguide containing a p-i-n diode with a reverse bias voltage of V .

III. EFFECTIVE CARRIER LIFETIME REDUCTION USING A REVERSELY BIASED p-i-n DIODE SILICON WAVEGUIDE

In the preceding section, we showed that TPA-induced FCA is a dominant factor limiting the maximum Raman gain obtainable in silicon waveguides. As the FCA is determined by the photo-generated free carrier density, it is critical to have a way to reduce the accumulated carrier density inside the waveguide in order to obtain net gain in silicon waveguide. In the following, we propose and demonstrate using a reversely biased p-i-n diode waveguide to reduce the TPA effect associated with Raman scattering.

Fig. 9 shows a schematic of a silicon waveguide containing a p-i-n diode with a reverse bias voltage. It consists of a regular silicon rib structure with a heavily doped p-type area and a heavily doped n-type area in the silicon slab region. The heavily doped regions insure good ohmic contacts between silicon and metal layers. The intrinsic carrier density in the SOI wafer should be as low as possible to ensure the applied reverse bias voltage creates a strong electric field in the waveguide center. The applied electric field will accelerate the motion of electrons and holes in the waveguide. The carrier transit time

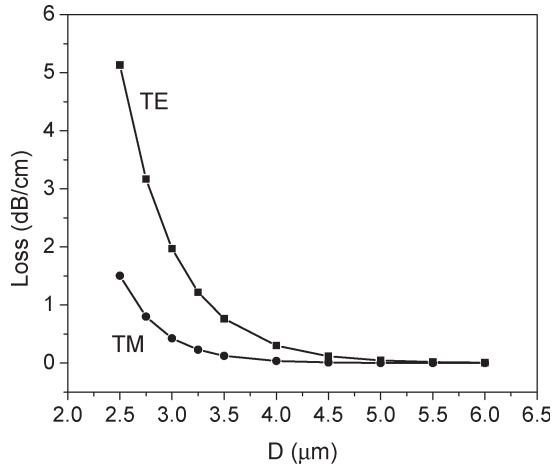


Fig. 10. Modeled TE and TM optical transmission losses of a silicon p-i-n diode waveguide as a function of the p- and n-doping separation D . Waveguide sidewall roughness scattering loss is not included in the simulation.

will determine the carrier density if it is shorter than the carrier recombination lifetime. To make the p-i-n diode waveguide viable for Raman amplification and lasing, one has to keep the linear optical transmission loss low while reducing the free carrier density inside the waveguide. As the carrier transit time across the waveguide depends on the p- and n-doping separation (D), one would intuitively like to minimize D for optimal device performance. However, the optical absorption loss due to the heavily doped regions increases when D is too small. Therefore, D is a critical parameter to be carefully considered for low-loss p-i-n devices. In the following, we first analyze the p- and n-doping separation effect on the waveguide loss and then show the bias voltage effect on the carrier density inside the waveguide.

We use a fully vectorial waveguide modal solver [53] to model optical loss as a function of the p- and n-doping separation D for a p-i-n diode waveguide. Results for both TE and TM modes are shown in Fig. 10. The modeled waveguide dimensions are rib width $W = 1.5 \mu\text{m}$, the rib height $H = 1.55 \mu\text{m}$, and slab height $h = 0.85 \mu\text{m}$. Our modeling suggests that such a waveguide is a single-mode device. For the p- and n-doped contact regions, a high concentration of $5 \times 10^{19} \text{ cm}^{-3}$ is used. The doping layer thickness is assumed to be $0.3 \mu\text{m}$. The light wavelength is $\lambda = 1550 \text{ nm}$. For the doping density dependent optical absorption, we used the formula [59]

$$\Delta\alpha_e = 8.5 \times 10^{-18} \Delta N_e \quad \Delta\alpha_h = 6.0 \times 10^{-18} \Delta N_h \quad (12)$$

where ΔN_e and ΔN_h are the n- and p-type doping concentration in units per cubic centimeter and the absorption coefficient is in units per centimeter. We see in Fig. 10 that optical loss due to the doping regions is negligible for both TE and TM modes unless the separation D is smaller than $4.5 \mu\text{m}$. We also note in Fig. 10 that the TE mode has a higher absorption as compared to the TM mode. This is due to the fact that the TM mode has a tighter lateral modal profile so that there is a smaller overlap between the doped regions and optical electrical field. Here, we want to mention that waveguide loss in Fig. 10 does not include waveguide sidewall roughness scattering loss. Including the scattering loss would not change the waveguide

loss dependence on the p- and n-doping separation, except that the overall transmission loss of the waveguide is increased.

To obtain a qualitative understanding of the reverse bias effect on the FCA in a p-i-n diode waveguide, we modeled the carrier density inside the waveguide generated by the TPA process as a function of the bias voltage by using a two-dimensional (2-D) semiconductor device simulation package called ATLAS/SILVACO [60]. In our modeling, the same waveguide geometry in Fig. 10 was used. For the intrinsic region, we assumed it is p type and has a doping concentration of $1 \times 10^{14} \text{ cm}^{-3}$ (since the doping concentration in the intrinsic region is very small, the final result is not dependent on the doping type). The heavily doped p- and n-region separation is $D = 6 \mu\text{m}$. In the case of reverse bias, the free carrier (electron-hole pair) generation in the p-i-n diode is due to the TPA process and the generation rate is given by [42], [57], [58]

$$G_r = \frac{\beta \lambda_p}{2hc} \frac{P^2}{A_{\text{eff}}^2} \quad (13)$$

where β is the TPA coefficient of silicon, λ_p is the pump wavelength, P is the pump power inside the silicon waveguide, and A_{eff} is the effective core area defined in (10). Here, we note that the pump intensity distribution is essentially determined by the optical mode. Therefore, the photocarrier generation rate is, in general, nonuniform across the waveguide. For simplicity, however, we assumed in (13) that it is constant inside the effective core area but zero outside the effective core area. To account for the free carrier decay process in silicon, the Shockley-Reed-Hall (SHR) carrier recombination model was used. The carrier lifetime is assumed to be $2 \mu\text{s}$ for both electrons and holes. As the carrier dynamics in the reversely biased p-i-n diode is essentially determined by the field-induced drifting, we found that the simulation results are very insensitive to the choice of the carrier lifetime. The carrier density dependent carrier mobility was also included in the device modeling package. After solving the coupled Poisson equation with free electron and hole continuity equations that incorporate both carrier generation and recombination rates, we obtain the carrier density inside the waveguide as well as other physical quantities. In Fig. 11, we plot the peak carrier density as a function of the reverse bias voltage for two different pump powers, namely, $P = 669$ and 945 mW . We chose the peak carrier density as a quantity to look at, because it leads to the peak FCA. To obtain a qualitative understanding of the reverse bias effect on the carrier density, we feel that it is enough to monitor how the peak carrier density depends on the bias. We see in Fig. 11 that, for a given pump power, the carrier density is significantly reduced when the bias voltage is increased. It is also interesting to note that the carrier density is not linearly dependent on the bias. The carrier density decreases rapidly when the bias voltage varies from 0 to 4–6 V. It changes slower when the bias voltage is higher. This is partly due to the field-dependent mobility and partly due to the free carrier screening effect on the applied field.

The above 2-D device modeling gives us a qualitative understanding of the reverse bias effect on the lateral motion of TPA-induced free carriers. However, the 2-D modeling does

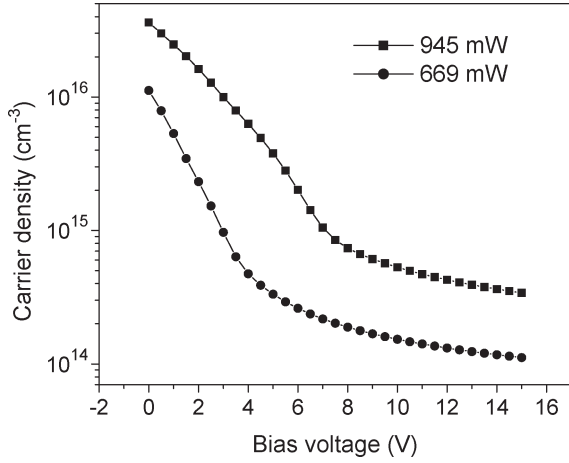


Fig. 11. Modeled carrier density inside a p-i-n diode waveguide as a function of the reverse bias voltage for two different pump powers, namely, $P = 669$ and 945 mW.

not take into account the longitudinal effect of the waveguide, in which the optical mode propagates. As a first-order approximation, we may assume that the lateral and longitudinal motion of the carrier is decoupled. Then, we could introduce an effective carrier lifetime to characterize the lateral motion of the carrier due to the reverse bias. In the presence of optical loss, the pump intensity is decaying along the light propagation direction. Thus, we also expect the TPA-induced carrier density is decaying as well. However, the effective carrier lifetime is only dependent on the bias but not the waveguide length. Based on these arguments, we could describe the nonlinear optical transmission in a waveguide using a one-dimensional propagation equation by introducing a bias-voltage-dependent carrier lifetime τ_{eff} . Taking into account the TPA and TPA-induced FCA, the optical power $P(z)$ evolution along the waveguide (z -direction) is governed by [42], [57]

$$\frac{dP(z)}{dz} = -\alpha P(z) - \frac{\beta}{A_{\text{eff}}} P^2(z) - \sigma N(z) P(z) \quad (14)$$

where σ is the FCA cross section, and $N(z)$ is the free carrier density. In the case of CW power injection, the carrier density in the waveguide is given by [42], [57], [58]

$$N(z) = \frac{\beta \lambda_p \tau_{\text{eff}}}{2hc} \frac{P^2(z)}{A_{\text{eff}}^2}. \quad (15)$$

Using a finite-difference method, we can readily solve coupled (14) and (15) for a given input pump power $P(0)$. Then, one can obtain the output power of the waveguide. Using a linear absorption loss of $\alpha = 0.22$ dB/cm, $\sigma = 1.45 \times 10^{-17}$ cm² [59], $\beta = 0.5$ cm/GW [38], [56], and $\tau_{\text{eff}} = 23$ ns, we obtained the solid curve in Fig. 7, which agrees well with experimental data.

To experimentally verify that one can reduce the TPA effect, we fabricated a p-i-n diode waveguide and measured nonlinear optical transmission as a function of the reverse bias. The scanning electron microscope (SEM) picture of the fabricated device is shown in Fig. 12. The waveguide has a rib width of $1.5 \mu\text{m}$, a rib height of $1.56 \mu\text{m}$, and an etch depth of

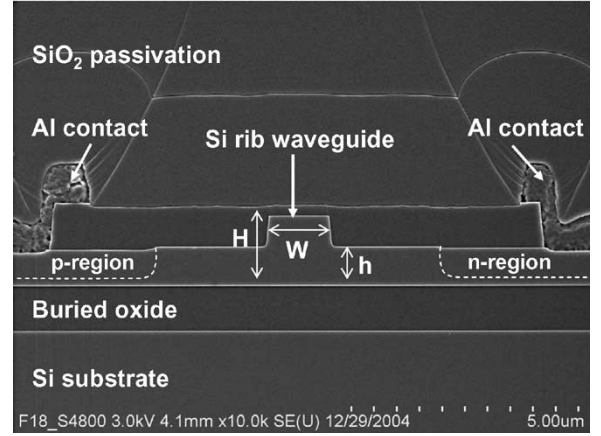


Fig. 12. SEM image of a p-i-n diode waveguide used for Raman amplification and lasing experiments.

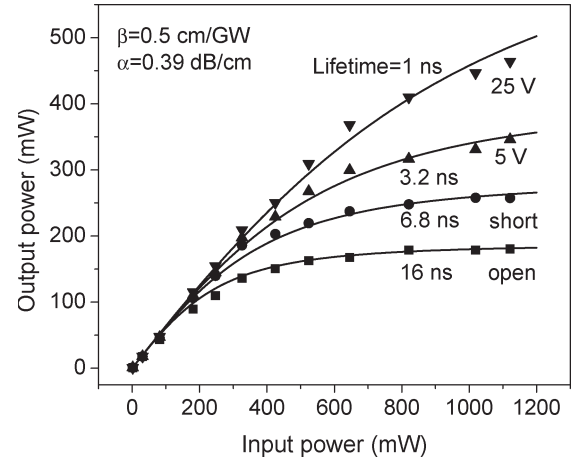


Fig. 13. Measured and modeled output power of a 4.8-cm-long p-i-n diode silicon waveguide as a function of input power at various bias voltages. The linear optical loss of the waveguide is $\alpha = 0.39$ dB/cm. The TPA coefficient is $\beta = 0.5$ cm/GW. The effective carrier lifetime is used as a fitting parameter for each bias.

$0.75 \mu\text{m}$. The p- and n-doping separation is $D = 6 \mu\text{m}$. We chose such a large separation to insure that doping regions have no contribution to the waveguide loss (see Fig. 10). The linear optical transmission loss of the waveguide was determined by the FP resonance technique. We found that the loss is 0.35 ± 0.1 dB/cm. This loss value is slightly higher than what we obtained for a similar waveguide size without p- and n- doping regions. It may be due to different surface roughness of the waveguides.

Fig. 13 shows both measured and modeled nonlinear optical transmission of a 4.8-cm-long p-i-n diode waveguide with different bias voltages. The symbols represent the experimental data and the solid curves represent the modeled results. The wavelength is $\lambda_p = 1550$ nm. As mentioned above, the effective carrier lifetime is dependent on the bias voltage. We therefore use it as a fitting parameter to fit the experimental data. The obtained effective carrier lifetime represents the measure of the applied electric field effect on the carrier dynamics. We see in Fig. 13 that there is generally a good agreement between the measurement and modeling. When the p-i-n diode is electrically open (no net current flow), a long lifetime of 16 ns

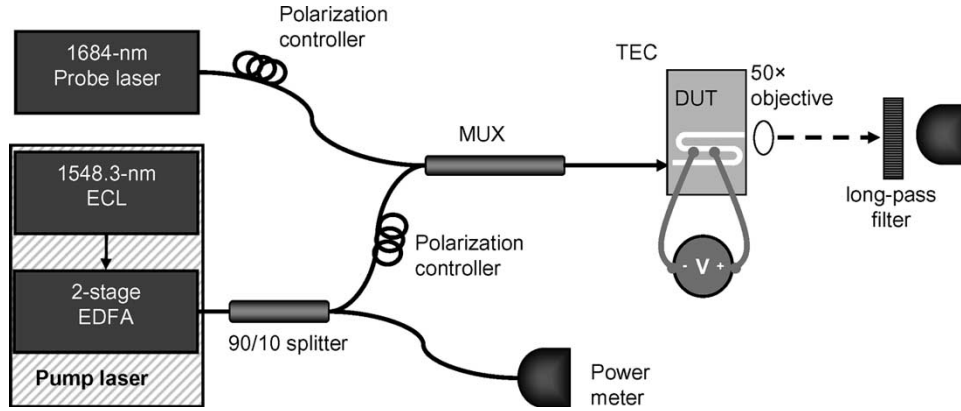


Fig. 14. Experimental setup used for net optical gain characterization of the p-i-n diode silicon waveguide.

is obtained. As a result, the optical transmission saturates at an output power of 180 mW. When the p-i-n diode is electrically closed (in this case, the net current flow is allowed), the carrier lifetime is reduced to 6.8 ns, and the optical transmission is increased. As the reverse bias is continuously increased, the carrier lifetime is further reduced and the optical transmission is increased. At a bias voltage of 25 V, we obtained a carrier lifetime of 1 ns. This represents an order of magnitude improvement in the carrier lifetime. Thus, we expect that the pump-induced optical loss can be largely suppressed and that net optical gain can be achieved. In the following section, we will describe our characterization of the net gain of the silicon p-i-n diode waveguide.

IV. NET OPTICAL GAIN DUE TO SRS IN SILICON WAVEGUIDE

In the preceding section, we showed that the TPA-induced FCA can be significantly reduced by introducing a reversely biased p-i-n diode in a silicon waveguide. We now characterize the Raman gain of the silicon waveguide by using a pump-probe experiment. The experimental setup is shown in Fig. 14, which is slightly different from Fig. 4. The pump and probe lasers are combined with a wavelength multiplexer into a lensed single-mode fiber whose output is used to couple to the waveguide under investigation. The output beam of the waveguide is collimated by a 50x objective lens, and a long-wavelength pass optical filter is used to separate the pump and probe beams. The probe beam passes through the filter and is detected with a photodetector while the pump beam is blocked by the filter. Fiber polarization controllers at the input to the device under test allow both probe and pump beam polarizations to be independently controlled. The device under test is mounted on a thermoelectric cooler (TEC) and kept at a constant temperature of 25 °C.

For the CW gain measurements, the pump laser is a CW tunable external cavity laser emitting around 1548.3 nm, which is amplified using two erbium-doped fiber amplifiers (EDFAs) to a maximum output power of 4 W. The probe laser is a 2-mW external cavity tunable diode laser operating at around 1684 nm. Both the pump and probe laser sources have linewidths of ≤ 100 MHz. The polarization directions of the probe and the pump beam are aligned with the TE mode of the waveguide.

To measure the maximum SRS gain, the transmitted probe power is measured at the peak of the Raman gain profile (at the Stokes wavelength) and compared to the input probe power. The input probe power is determined from the measured transmitted probe power without the pump beam by factorizing out the linear transmission loss of the waveguide.

In the pump-probe experiment, we used the same silicon waveguide used for the nonlinear transmission measurements in Fig. 13. Therefore, the effective carrier lifetimes deduced from Fig. 13 for various bias voltages can also be used to describe the pump-probe experiment. Since the probe power is low, we ignore the pump depletion in the description of the pump-probe experiment. Taking into account the TPA and TPA-induced FCA at the Stokes wavelength, the probe power $[P_s(z)]$ in the waveguide can be described by [32], [42], [57]

$$\frac{dP_s(z)}{dz} = -\alpha P_s(z) - \frac{2\beta - g_r}{A_{\text{eff}}} P(z) P_s(z) - \sigma N(z) P_s(z). \quad (16)$$

Solving (16) using the pump power obtained from (14) and with probe input power $P_s(0)$ as an initial condition, one obtains the net optical gain of the waveguide via

$$G = 10 \log \frac{P_s(L)}{P_s(0)} \quad (17)$$

where $P_s(L)$ is the probe output power obtained from (16), and L is the waveguide length.

Fig. 15 shows the net CW Raman gain as a function of the pump power inside the waveguide for a 4.8-cm-long waveguide at various bias voltages. The pump power is the power of the pump coupled into the waveguide and is determined by measuring the power exiting the lensed fiber and factorizing out coupling loss to the waveguide. The symbols represent the experimental data, and the curves are the modeled results. In the modeling, we used a linear loss of 0.39 dB/cm. At the Stokes wavelength of 1684 nm, the FCA cross section is $\sim 1.71 \times 10^{-17} \text{ cm}^2$ [59]. The only fitting parameter is the gain coefficient g_r . We see in Fig. 15 that there is no net gain when the p-i-n diode is open. This is due to the fact that when the carrier lifetime is long, the Raman gain cannot compensate for

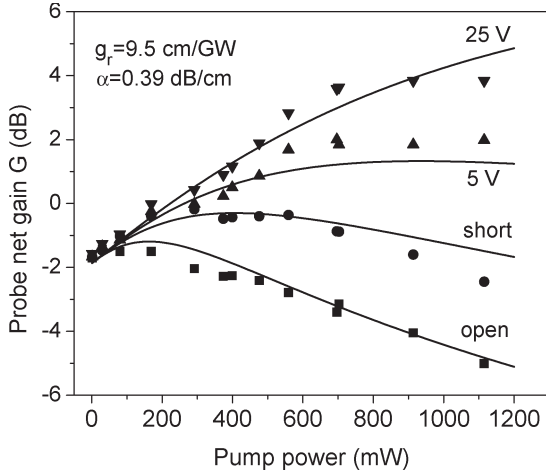


Fig. 15. Measured and modeled probe net gain of a p-i-n diode waveguide at different bias voltages. In the modeling, the same parameters as in Fig. 13 are used, except that the Raman gain coefficient g_r is used as a fitting parameter.

the loss due to the linear waveguide scattering loss, TPA, and TPA-induced FCA. When the diode is short circuited, the FCA is significantly reduced, but there is still no net gain observed. Once the p-i-n is reversely biased, net gain is achieved. With a reverse bias of 5 V, we obtained a net gain of ~ 2 dB with a pump power of ~ 700 mW. Using a higher bias voltage of 25 V, a net gain of > 3 dB is achieved for pump powers above 700 mW. With predetermined linear and nonlinear optical loss of the waveguide, one is able to determine the Raman gain coefficient by comparing measured and modeled net gain. Using a common gain coefficient of $g_r = 9.5$ cm/GW, the modeled net gain agrees relatively well with the experimental data for various reverse bias voltages and pump powers. In passing, we notice that there is a range of Raman gain coefficient values reported in the literature obtained using both spontaneous Raman scattering and pump-probe measurements for different size waveguides [37]–[40], [44]. The cause of such a large variation in the Raman gain coefficient is not clear. For a better understanding, further investigation is needed.

As the SRS gain spectrum of silicon waveguides without the p-i-n diode is relatively narrow (see Fig. 5), we expect that the net gain decreases when the pump and probe frequency difference is tuned away from the Stokes shift of 15.6 THz. Fig. 16 shows the measured net Raman gain as a function of the pump wavelength at a fixed probe wavelength of 1684 nm. In the measurement, the p-i-n bias was set at 25 V and the pump power at 511 mW. We see in Fig. 16 that net Raman gain is observed over the 0.5-nm wavelength range for a pump power of 511 mW. We expect that the net gain window becomes wider with a higher pump power. Fig. 16 also shows that the 3-dB linewidth of the SRS spectrum is ~ 100 GHz, which is consistent with Fig. 5(b).

With the ability of achieving net CW gain in silicon waveguides, we performed an experiment to measure amplification of a modulated square-wave optical signal at 5 GHz as it passed through the reversely biased p-i-n diode waveguide. Fig. 17 shows the probe output signal of a 4.8-cm-long silicon waveguide with different pump levels, namely, $P = 280$,

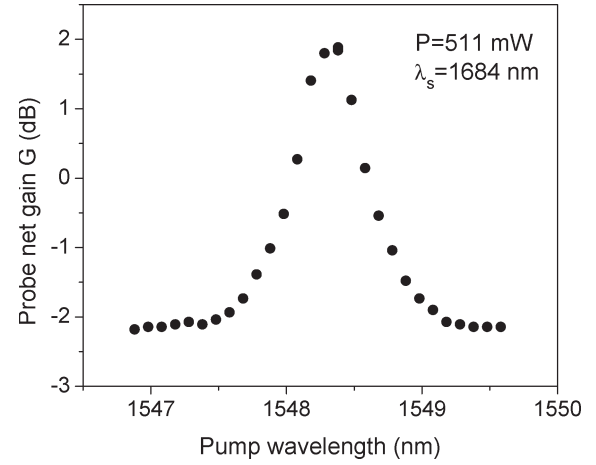


Fig. 16. Measured probe net gain as a function of the pump wavelength at a pump power of $P = 511$ mW. The probe wavelength is fixed at $\lambda_s = 1684$ nm.

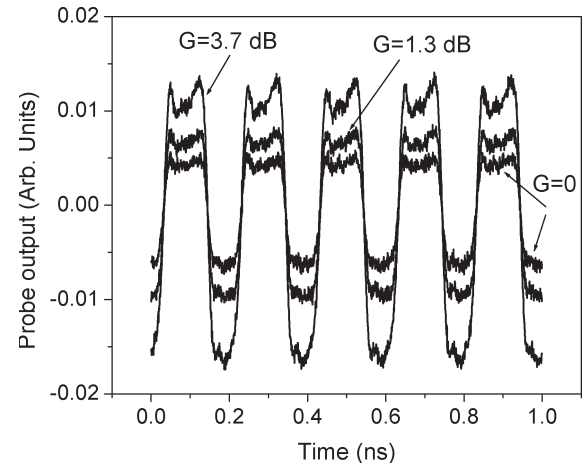


Fig. 17. Probe output signals of a 4.8-cm-long silicon waveguide for three different pump powers, i.e., $P = 280$, 380, and 724 mW. The corresponding probe net gain is $G = 0$, 1.3, and 3.7 dB. The reverse bias voltage is 25 V.

380, and 724 mW. The corresponding net gain of the waveguide is $G = 0$, 1.3, and 3.7 dB. The reverse bias voltage is 25 V. With a pump wavelength of 1550 nm, the Stokes (signal) wavelength is around 1686 nm. Since the modulator and detector used for these measurements were designed for the C- and L-band, their performance and sensitivity are degraded at the signal wavelength, resulting in somewhat distortion of the probe signal before coupled into the silicon waveguide. To verify the signal integrity after being amplified, we compared the amplified signal (with a 3.7-dB net gain) to the input signal. In Fig. 18, we plot both the input and output signals normalized to have the same signal amplitude. We see in Fig. 18 that the shapes of the input and output signals are almost identical. There is no distortion for both rising and falling edges of the square wave signal. The rise/fall time of < 40 ps suggests that the silicon Raman amplifier is capable of amplifying the light carrying data streams with transfer rate of at least 10 Gb/s. However, further experiment on the Raman response time of silicon is needed to determine the ultimate bit rate limit of the silicon Raman amplifier.

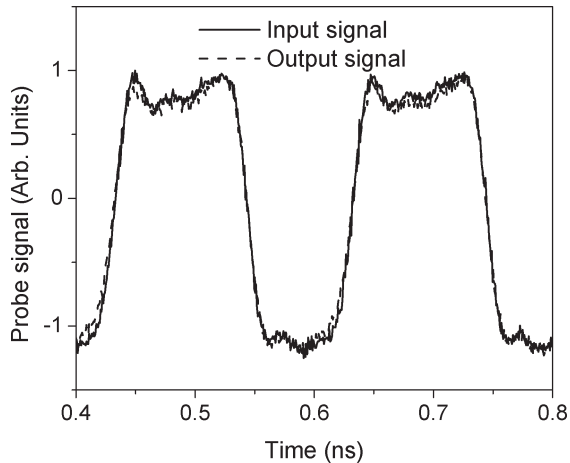


Fig. 18. Input probe signal (solid curve) and output probe signal (dashed curve) passing through the p-i-n diode silicon waveguide with a pump power of 724 mW giving a net gain of $G = 3.7$ dB. For rise/fall edge comparison, the output signal is normalized to have the same amplitude as for the input signal.

V. RAMAN SILICON LASER

After obtaining a sizable net optical gain in a silicon waveguide, one could achieve lasing when an optical feedback is added to the gain medium. In this section, we describe our design and experiment of all-silicon Raman laser. Both pulsed and CW lasing operations are discussed.

The silicon Raman laser described here is based on the same low-loss single-mode rib waveguide containing a reversely biased p-i-n diode structure we used for our net gain characterization. The silicon Raman laser optical cavity was formed by coating one of the waveguide facets with a multilayer coating while leaving the other facet uncoated. The facet coating was designed to be broadband and have a high reflectivity ($\sim 90\%$) for both the pump wavelength of $1.536 \mu\text{m}$ and the Raman/Stokes wavelength of $1.67 \mu\text{m}$. The uncoated facet has a reflectivity of $\sim 30\%$ for both pump and Raman wavelengths. The pump beam is coupled into the cavity through the uncoated facet. Although the laser beam is emitted from both facets of the silicon chip, we measured the laser output only from the uncoated facet. The waveguide loss was measured before the application of the multilayer coating to the waveguide facet. The coating reflectivity was determined by measuring the linear optical transmission spectrum of the same waveguides before and after application of the coating.

Fig. 19 shows the experimental setup. An external cavity CW diode laser at $1.536 \mu\text{m}$ is amplitude modulated using an acoustooptic modulator to produce square-wave pulses of ~ 130 ns width at 10 kHz. An EDFA system of three gain stages is used to amplify these pulses to produce a pump beam of peak power up to 2 W. The pump beam passes through a thin-film-based wavelength demultiplexer and is coupled into the waveguide cavity by a lensed fiber. The Raman laser output and the reflected pump beam are coupled back into the lensed fiber and separated through the wavelength demultiplexer. The extracted laser output from the reflection port of the demultiplexer is further filtered by a double-grating monochromator before being detected by a power meter or photodetector. The

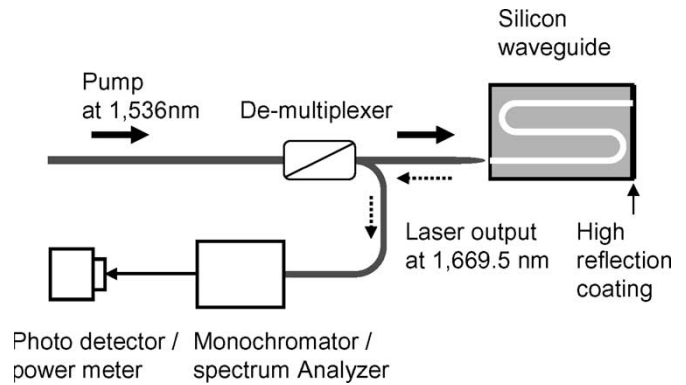


Fig. 19. Experimental setup used for pulsed all-silicon Raman lasing measurement.

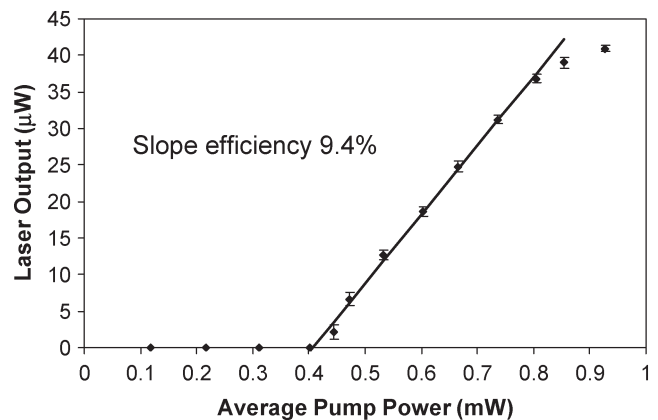


Fig. 20. Averaged laser output power as a function of the averaged pump power for an all-silicon Raman laser with a pulsed pumping.

coupling loss between the lensed fiber and the waveguide was measured to be ~ 4 dB, the insertion loss of the demultiplexer is 0.6 dB, and the monochromator has a loss of 6.7 dB.

Fig. 20 shows the average power of the laser output measured from the uncoated side of the silicon waveguide cavity with a reverse bias of 25 V as a function of average pump power into the waveguide cavity. As can be seen in Fig. 20, the laser threshold is at ~ 0.4 mW, and the slope efficiency (single side output) is 9.4%. Including the laser output from the other facet with 90% reflectivity, we estimate the total slope efficiency to be $\sim 10\%$. At a pump power > 0.9 mW, the laser output starts to saturate. This mainly results from the fact that the free carrier lifetime is of the order of ~ 1 ns and nonlinear loss due to the TPA-induced FCA reduces the net gain at high pump powers.

At a pump power of 0.7 mW, we measured the spectrum of the Raman laser from the waveguide cavity. Fig. 21 shows a higher resolution spectrum of the laser using a scanning FP spectrum analyzer. We see that the laser has multiple cavity modes with one dominant mode. The mode spacing is measured to be ~ 0.9 GHz, which corresponds to the free spectral range of a 4.8-cm-long silicon waveguide cavity.

To obtain CW lasing operation, we modified our optical cavity design. To reduce the cavity loss at the Stokes wavelength, we coated both facets of the low-loss silicon waveguide with multilayer dielectric films. The front facet coating is dichroic,

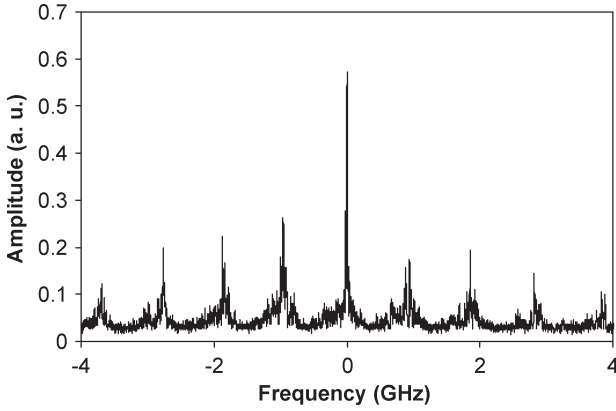


Fig. 21. Measured output spectrum of a pulsed all-silicon Raman laser at a pump power of 400 mW.

having a reflectivity of $\sim 71\%$ for the Raman/Stokes wavelength of 1686 nm and $\sim 24\%$ for the pump wavelength of 1550 nm. The back facet has a broadband high-reflectivity coating of $\sim 90\%$ for both pump and Raman wavelengths (Fig. 22). These waveguide facet reflectivities were determined by using the FP resonance technique [1]. The high reflectivities for the Stokes wavelength reduces the cavity loss so that CW lasing is achievable.

The experimental setup used for the CW lasing measurement is very similar to that used for the pulsed lasing experiment. Fig. 22 is a schematic of the CW Raman laser experiment. A CW external cavity diode laser (ECDL) at 1550 nm is amplified by an EDFA system to produce a pump beam of up to 3 W. The pump beam passes through a polarization controller followed by a thin-film-based wavelength demultiplexer and is coupled into the waveguide cavity by a lensed fiber through the front facet with the dichroic coating. The Raman laser output and the reflected pump beam are coupled back into the lensed fiber and separated through the wavelength demultiplexer. The extracted laser output from the reflection port of the demultiplexer is further filtered by a long wavelength pass (LP) filter before being detected by a power meter or optical spectrum analyzer. The coupling loss between the lensed fiber and the waveguide was measured to be ~ 4 dB and the insertion loss of the demultiplexer, and the long-pass filter is ~ 0.6 dB. The silicon chip is mounted on a TEC and kept at a constant temperature of 25°C .

At the pump wavelength, a low finesse cavity is formed by the high-reflectivity back facet and low-reflectivity front facet. This configuration allows us to utilize the cavity enhancement effect of the pump power to lower the lasing threshold. When the pump laser is tuned to the resonance of the cavity, the circulating power inside the waveguide cavity is enhanced. Consequently, we expect the lasing threshold to be lower as compared to the case where there is no cavity enhancement. To account for the cavity enhancement effect on the nonlinear optical interaction among the forward (+) and backward (−) propagating waves at both pump and Stokes wavelengths, we extend the rate-equation approach that was adopted in previous studies of Raman fiber lasers [61]–[63] to the silicon laser. Denoting the pump and Stokes amplitudes (optical power is equal to the square of the amplitude) A_p and A_s , respectively,

the equations that govern the evolution of the pump and Stokes waves read as [64]

$$\begin{aligned} \pm \frac{dA_p^\pm}{dz} &= \left[-\frac{g_r}{2A_{\text{eff}}} \frac{\lambda_s}{\lambda_p} (A_s^{+2} + A_s^{-2}) - \frac{\alpha_p}{2} \right. \\ &\quad \left. - \frac{\beta}{2A_{\text{eff}}} (A_p^{\pm 2} + 2A_s^{+2} + 2A_s^{-2} + 2A_p^{\pm 2}) - \frac{\sigma_p}{2} N_{\text{eff}} \right] A_p^\pm \end{aligned} \quad (18)$$

$$\begin{aligned} \pm \frac{dA_s^\pm}{dz} &= \left[\frac{g_r}{2A_{\text{eff}}} (A_p^{+2} + A_p^{-2}) - \frac{\alpha_s}{2} \right. \\ &\quad \left. - \frac{\beta}{2A_{\text{eff}}} (A_s^{\pm 2} + 2A_p^{+2} + 2A_p^{-2} + 2A_s^{\pm 2}) - \frac{\sigma_s}{2} N_{\text{eff}} \right] A_s^\pm \end{aligned} \quad (19)$$

where α_p and α_s are the linear optical absorption coefficients of the waveguide at the pump and Stokes wavelengths, σ_p and σ_s are the FCA cross sections at the pump and Stokes wavelengths, respectively, and N_{eff} is the pump- and Raman-beam-induced free carrier density. In the vicinity of the lasing threshold, the Stokes amplitude is much smaller than the pump amplitude, it is reasonable to assume that the free carrier density is mainly due to the pump field. Then, the carrier density is given by [64]

$$N_{\text{eff}} = \frac{\beta \lambda_p \tau_{\text{eff}}}{2hcA_{\text{eff}}^2} [A_p^{+4} + A_p^{-4} + 2A_p^{+2}A_p^{-2}]. \quad (20)$$

To describe the steady state of our Raman silicon laser, the rate equations are supplemented by the boundary conditions enumerated as

$$A_p^+(0) = \sqrt{1 - R_{1p}} A_{\text{inc}} + \sqrt{R_{1p}} A_p^-(0) \quad (21)$$

$$A_p^-(L) = \sqrt{R_{2p}} A_p^+(L) \quad (22)$$

$$A_s^+(0) = \sqrt{R_{1s}} A_s^-(0) \quad (23)$$

$$A_s^-(L) = \sqrt{R_{2s}} A_s^+(L) \quad (24)$$

where A_{inc} is the incident pump amplitude, R_{1p} and R_{2p} are the front and back mirror reflectivities at the pump wavelength, and R_{1s} and R_{2s} are the front and back mirror reflectivities at the Stokes wavelength. Note that our formulism is different from what was used in [65], since we solve for the optical field amplitude instead of the power. Using our formulism, we can obtain the same cavity enhancement factor at the FP resonance (i.e., under the condition that the half-round-trip phase is $m\pi$, m being an integer) as has been reported in the literature [66]. We solve coupled (18)–(20) using a finite element technique combining with the boundary conditions above. In passing, we note that the spontaneous Raman scattering is not included in our formulism. Therefore, there is no nonzero solution for the Stokes wave when the pump power is low. The lasing occurs when a nonzero solution of the Stokes wave is found at a

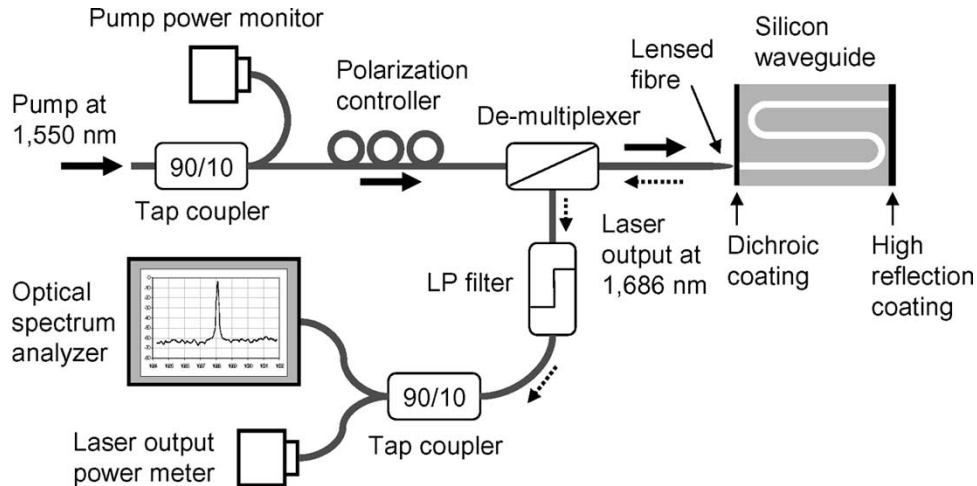


Fig. 22. Experimental setup used for the CW all-silicon Raman lasing measurement.

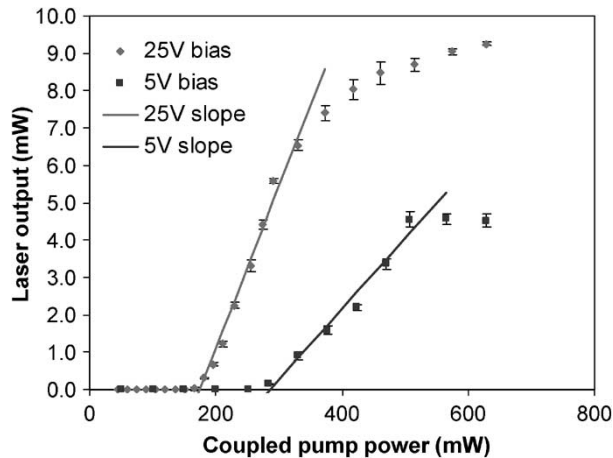


Fig. 23. Laser output power as a function of the coupled input power at two different bias voltages.

certain pump power. The corresponding power is defined as the threshold.

Fig. 23 plots the CW Raman laser output power versus the input pump power coupled into the laser cavity at two different reverse bias voltages applied to the p-i-n diode. In the experiment, the pump beam polarization is adjusted with a polarization controller, and its wavelength is fine tuned to the cavity resonance to maximize the laser output. The Raman laser frequency is 15.6 THz lower than that of the pump laser. We see in Fig. 23 that the lasing threshold changes with increasing bias voltage applied to the p-i-n. The lasing threshold is ~ 180 mW with a 25-V bias and ~ 280 mW with a 5-V bias. The lower threshold and higher laser output power with higher bias voltage is expected, because the effective carrier lifetime is shorter so that the nonlinear loss is lower, as shown in Fig. 13 [47]. Using the abovementioned cavity mirror reflectivities, linear optical loss of the waveguide, TPA coefficient, and the Raman gain coefficient of $g_r = 9.5$ cm/GW, we modeled the laser threshold. We found that the lasing threshold is expected to be ~ 182 and ~ 273 mW for a reverse bias of 25 and 5 V, respectively, which agrees well with the measurements. Note that excess nonlinear loss at higher pump power reduces the power enhancement effect and therefore increases the threshold

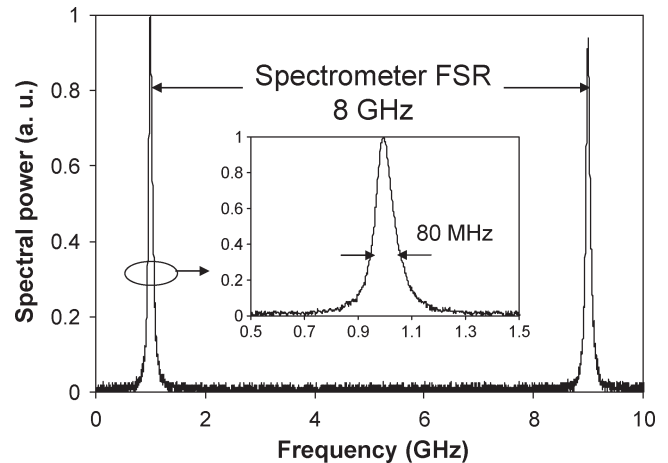


Fig. 24. Measured laser spectrum of the CW silicon Raman laser using a scanning FP spectrum analyzer.

pump power. The slope efficiency (single side output) above threshold is $\sim 4.3\%$ with a reverse bias of 25 V and 2% with a 5-V reverse bias. In Fig. 23 one sees that, for a pump power > 400 mW with a 25-V bias and for a pump power > 500 mW with a 5-V bias, the laser output begins to saturate. This is primarily due to the fact that the nonlinear loss due to the TPA-induced FCA reduces the net gain at higher pump powers, since the carrier lifetime of the p-i-n waveguide device is not reduced to zero. In addition, the cavity enhancement for the pump intensity reduces with increasing nonlinear loss, lowering the effective pump power in the cavity.

The spectrum of the laser output was measured with a confocal scanning FP spectrum analyzer with a free spectral range of 8 GHz and finesse of 100. Fig. 24 shows the Raman laser spectrum measured at a pump power of ~ 400 mW. We can see that the laser exhibits only a single mode; i.e., no other cavity modes with the expected mode spacing of 0.9 GHz for a 4.8-cm-long silicon waveguide cavity appear within the free spectral range (8 GHz) of the spectrum analyzer (see Fig. 21 for the multiple cavity modes). The measured linewidth of 80 MHz is limited by the resolution of the spectrum analyzer.

Fig. 25 is a plot of the laser output spectrum measured with a grating-based optical spectrum analyzer at various pump

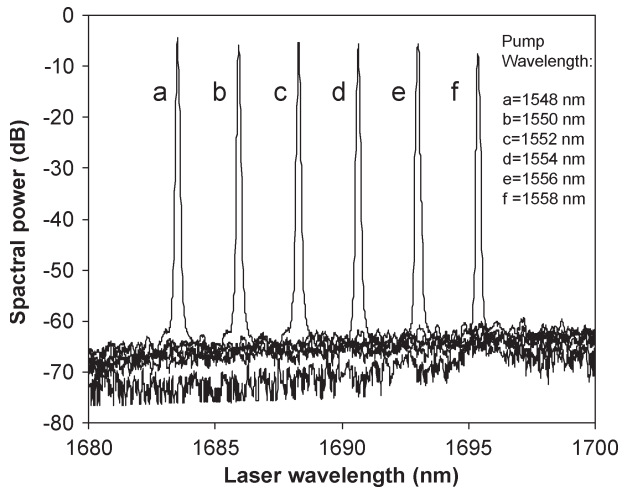


Fig. 25. Output spectra of a CW all-silicon Raman laser with various pump wavelengths.

wavelengths. The spectra shown were obtained by changing the wavelength of the pump laser seed (ECDL) from 1548 to 1558 nm in 2-nm steps. The input pump power was ~ 400 mW and a reverse bias of 25 V was applied to the p-i-n. We can see that the Raman laser output has over 55 dB side mode suppression, and its center wavelength corresponds to the appropriate Stokes wavelength for each pump wavelength. The displayed linewidth is limited by the resolution (0.07 nm) of the spectrum analyzer.

The demonstration of the CW Raman lasing in silicon represents a significant milestone in moving towards producing fully integrated monolithic photonic chips. However, the silicon laser device described above was by no means optimized for high performance. For future applications, the Raman silicon laser performance could be improved by device optimization. For example, optical cavity mirror and cavity length design could be optimized for higher conversion efficiency. The threshold power can be reduced by using a waveguide with smaller cross sectional dimensions and/or by introducing a larger cavity enhancement for the pump beam. In addition, with optimization of the p-i-n diode design, it is possible to further reduce the effective carrier lifetime to below 1 ns, which would reduce the saturation effect and, thus, increase the laser output power. The multilayer coating approach can also be replaced with waveguide Bragg reflectors or ring resonator architectures; both these alternatives are compatible with CMOS processing and could provide a platform for monolithic integration of silicon-based optoelectronics.

SRS in silicon could find potential applications in various areas ranging from communications to sensors and biomedicine. In the communications arena, silicon Raman amplifier can be used to amplify data or recover some of the optical losses incurred from integration of multiple silicon photonic devices. Lossless modulation in silicon has already been demonstrated [67]. Raman-induced four-wave mixing in silicon can be used for wavelength conversion from 1.55 to 1.30 μm wavelength bands [68]. Because the conversion is based on parametric Stokes to anti-Stokes coupling, achieving phase matching is critical to obtain high conversion efficiency for practical

applications. As the Stokes Raman scattering involves the conversion of a pump beam to a longer wavelength radiation, it could be used to create new laser sources at wavelengths that cannot be attained by compact semiconductor lasers at room temperature. In particular, it would be possible to generate light having wavelengths greater than 2 μm using multiple Stokes scattering scheme [69], [70] with an available optical pump source, because the Stokes frequency shift in silicon is relatively large. This is of interest in potential medical applications where water absorption peaks are located at 2.1 and 2.9 μm . Compared to cascaded Raman fiber lasers [69], [70], silicon lasers have the advantage of compactness and potentially low threshold with small waveguide dimensions. As a result, it is possible to integrate the silicon laser with other photonic devices such as silicon modulators to provide a low-cost single-chip solution for gas sensing and/or chemical absorption spectroscopy applications. Because low-loss silicon waveguides and high-performance Bragg gratings are critical for the cascaded Raman silicon laser, fabricating such a device is challenging. Significant technical development is required.

VI. SUMMARY

We have presented research results of the Raman scattering in a silicon waveguide. We outlined the fundamental physics associated with SRS in a silicon waveguide. We showed that nonlinear optical absorption due to the TPA-induced FCA is a dominant loss mechanism to limit the optical gain in the silicon waveguide. We designed and fabricated a low-loss silicon waveguide containing a p-i-n diode. We demonstrated both theoretically and experimentally that the free carrier density inside the waveguide can be reduced significantly with a reverse bias. As a result, the FCA loss is largely reduced, and we achieved net optical gain in silicon. Using this low-loss waveguide, we designed and fabricated a Raman silicon laser. Both pulsed and CW lasing operations were obtained. For the pulsed operation, we obtained a slope efficiency of $\sim 10\%$, while the slope efficiency is $\sim 5\%$ for the CW laser. As the effective carrier lifetime of our reversely biased p-i-n diode waveguide is ~ 1 ns, the nonlinear optical loss associated with the TPA-induced FCA is still noticeable under the high-power pumping. Improving the p-i-n diode waveguide design may further reduce the TPA-induced FCA and enhance the laser conversion efficiency. We also showed that the cavity enhancement of the pump beam lowers the threshold. As the silicon Raman laser was fabricated with CMOS-compatible technology, our achievement shows the potential of monolithic integration of silicon-based optoelectronics.

ACKNOWLEDGMENT

The authors thank A. Alduino, D. Tran, J. Tseng, A. Fang, D. Hodge, and J. Johnson for assistance in device fabrication and sample preparation, S. Koehl for software development, M. Morse, H. Liu, M. Salib, D. Samararubio, and L. Liao for technical discussions, and G. T. Reed, I. P. Kaminow, and J. E. Bowers for helpful conversations.

REFERENCES

- [1] G. T. Reed and A. P. Knights, *Silicon Photonics: An Introduction*. Chichester, U.K.: Wiley, 2004.
- [2] *Silicon Photonics*, vol. 94, *Topics in Appl. Phys.*, L. Pavesi and D. J. Lockwood, Eds. Berlin, Germany: Springer-Verlag, 2004.
- [3] A. Liu, R. Jones, L. Liao, D. Samara-Rubio, D. Rubin, O. Cohen, R. Nicolaescu, and M. Paniccia, "A high-speed silicon optical modulator based on a metal-oxide-semiconductor capacitor," *Nature*, vol. 427, no. 6975, pp. 615–618, Feb. 2004.
- [4] L. Liao, D. Samara-Rubio, M. Morse, A. Liu, D. Hodge, D. Rubin, U. D. Keil, and T. Franck, "High-speed silicon Mach-Zehnder modulator," *Opt. Express*, vol. 13, no. 8, pp. 3129–3135, Apr. 2005.
- [5] L. Naval, B. Jalali, L. Gomelsky, and J. M. Liu, "Optimization of $\text{Si}_{1-x}\text{Ge}_x/\text{Si}$ waveguide photodetectors operating at $\lambda = 1.3 \mu\text{m}$," *J. Lightw. Technol.*, vol. 14, no. 5, pp. 787–797, May 1996.
- [6] L. Colace, G. Masini, and G. Assanto, "Ge-on-Si approach to the detection of near-infrared light," *IEEE J. Quantum Electron.*, vol. 35, no. 12, pp. 1843–1852, Dec. 1999.
- [7] L. T. Canham, "Silicon quantum wire array fabrication by electrochemical and chemical dissolution of wafers," *Appl. Phys. Lett.*, vol. 57, no. 10, pp. 1046–1048, Sep. 1990.
- [8] V. Lehmann and U. Gösele, "Porous silicon formation: A quantum wire effect," *Appl. Phys. Lett.*, vol. 58, no. 8, pp. 856–858, Feb. 1991.
- [9] K. Chen, X. Huang, J. Xu, and D. Feng, "Visible photoluminescence in crystallized amorphous Si:H/SiN_x : H multiquantum-well structures," *Appl. Phys. Lett.*, vol. 61, no. 17, pp. 2069–2071, Oct. 1992.
- [10] T. Shimizu-Iwayama, K. Fujita, S. Nakao, K. Saitoh, T. Fujia, and N. Itoh, "Visible photoluminescence in Si^+ -implanted silica glass," *J. Appl. Phys.*, vol. 75, no. 12, pp. 7779–7783, Jun. 1994.
- [11] G. G. Qin, A. P. Li, B. R. Zhang, and B. C. Li, "Visible electroluminescence from semitransparent Au film/extra thin Si-rich silicon oxide film/p-Si structure," *J. Appl. Phys.*, vol. 78, no. 3, pp. 2006–2009, Aug. 1995.
- [12] M. Wang, X. Huang, J. Xu, W. Li, Z. Liu, and K. Chen, "Observation of the size-dependent blueshifted electroluminescence from nanocrystalline Si fabricated by KrF excimer laser annealing of hydrogenated amorphous silicon/amorphous- SiN_x : H superlattices," *Appl. Phys. Lett.*, vol. 72, no. 6, pp. 722–724, Feb. 1998.
- [13] M. L. Brongersma, A. Polman, K. S. Min, T. Tambo, and H. A. Atwater, "Tuning the emission wavelength of Si nanocrystals in SiO_2 by oxidation," *Appl. Phys. Lett.*, vol. 72, no. 20, pp. 2577–2579, May 1998.
- [14] F. Iacona, G. Franzo, and C. Spinella, "Correlation between luminescence and structural properties of Si nanocrystals," *J. Appl. Phys.*, vol. 87, no. 3, pp. 1295–1303, Feb. 2000.
- [15] G. F. Grom, D. J. Lockwood, J. P. McCaffrey, H. J. Labbe, P. M. Fauchet, B. White, Jr., J. Diener, D. Kovalev, F. Koch, and L. Tsybeskov, "Ordering and self-organization in nanocrystalline silicon," *Nature*, vol. 407, no. 6802, pp. 358–361, Sep. 2000.
- [16] L. Pavesi, L. D. Negro, C. Mazzoleni, G. Franzo, and F. Priolo, "Optical gain in silicon nanocrystals," *Nature*, vol. 408, no. 6811, pp. 440–444, Nov. 2000.
- [17] L. Khriachtchev, M. Rasanen, S. Novikov, and J. Sinkkonen, "Optical gain in Si/SiO_2 lattice: Experimental evidence with nanosecond pulses," *Appl. Phys. Lett.*, vol. 79, no. 9, pp. 1249–1251, Aug. 2001.
- [18] L. Dal Negro, M. Cazzanelli, L. Pavesi, S. Ossicini, D. Pacifici, G. Franzo, F. Priolo, and F. Iacona, "Dynamics of stimulated emission in silicon nanocrystals," *Appl. Phys. Lett.*, vol. 82, no. 26, pp. 4636–4638, Jun. 2003.
- [19] J. Ruan, P. M. Fauchet, L. Dal Negro, M. Cazzanelli, and L. Pavesi, "Stimulated emission in nanocrystalline silicon superlattices," *Appl. Phys. Lett.*, vol. 83, no. 26, pp. 5479–5481, Dec. 2003.
- [20] L. Dal Negro, M. Cazzanelli, B. Danese, L. Pavesi, F. Iacona, G. Franzo, and F. Priolo, "Light amplification in silicon nanocrystals by pump and probe transmission measurements," *J. Appl. Phys.*, vol. 96, no. 10, pp. 5747–5755, Nov. 2004.
- [21] S. Lombardo, S. U. Campisano, G. N. van den Hoven, A. Cacciato, and A. Polman, "Room-temperature luminescence from Er^{3+} -implanted semi-insulating polycrystalline silicon," *Appl. Phys. Lett.*, vol. 63, no. 14, pp. 1942–1944, Aug. 1993.
- [22] M. Fujii, M. Yoshida, Y. Kanzawa, S. Hayashi, and K. Yamamoto, "1.54 μm photoluminescence of Er^{3+} doped into SiO_2 films containing Si nanocrystals: Evidence for energy transfer from Si nanocrystals to Er^{3+} ," *Appl. Phys. Lett.*, vol. 71, no. 9, pp. 1198–1200, Sep. 1997.
- [23] G. Franzo, S. Coffa, F. Priolo, and C. Spinella, "Mechanism and performance of forward and reverse bias electroluminescence at 1.54 μm from Er-doped Si diodes," *J. Appl. Phys.*, vol. 81, no. 6, pp. 2784–2793, Mar. 1997.
- [24] F. Priolo, G. Franzo, S. Coffa, and A. Carnera, "Excitation and nonradiative deexcitation processes of Er^{3+} in crystalline Si," *Phys. Rev. B, Condens. Matter*, vol. 57, no. 8, pp. 4443–4455, Feb. 1998.
- [25] P. G. Kik, M. L. Brongersma, and A. Polman, "Strong exciton-erbium coupling in Si nanocrystal-doped SiO_2 ," *Appl. Phys. Lett.*, vol. 76, no. 17, pp. 2325–2327, Apr. 2000.
- [26] H. S. Han, S. Y. Seo, and J. H. Shin, "Optical gain at 1.54 μm in erbium-doped nanocluster sensitized waveguide," *Appl. Phys. Lett.*, vol. 79, no. 27, pp. 4568–4570, Oct. 2001.
- [27] F. Iacona, D. Pacifici, A. Irrera, M. Miritello, G. Franzo, F. Priolo, D. Sanfilippo, G. Di Stefano, and P. G. Fallica, "Electroluminescence at 1.54 μm in Er-doped Si nanocluster-based devices," *Appl. Phys. Lett.*, vol. 81, no. 17, pp. 3242–3244, Oct. 2002.
- [28] W. L. Ng, M. A. Lourenco, R. M. Gwilliam, S. Ledain, G. Shao, and K. P. Homewood, "An efficient room-temperature silicon-based light-emitting diode," *Nature*, vol. 410, no. 6825, pp. 192–194, Mar. 2001.
- [29] T. Trupke, J. Zhao, A. Wang, R. Corkish, and M. Green, "Very efficient light emission from bulk crystalline silicon," *Appl. Phys. Lett.*, vol. 82, no. 18, pp. 2996–2998, May 2003.
- [30] K. P. Homewood and M. A. Lourenco, "Light from Si via dislocation loops," *Mater. Today*, vol. 8, no. 1, pp. 34–39, Jan. 2005.
- [31] G. Dehlinger, L. Diehl, U. Gennser, H. Sigg, J. Faist, K. Ensslin, and D. Grutzmacher, "Intersubband electroluminescence from silicon-based quantum cascade structures," *Science*, vol. 290, no. 5500, pp. 2277–2280, Dec. 2000.
- [32] G. P. Agrawal, *Nonlinear Fiber Optics*, 2nd ed. New York: Academic, 1995.
- [33] J. P. Russell, "Raman scattering in silicon," *Appl. Phys. Lett.*, vol. 6, no. 11, pp. 223–224, Jun. 1965.
- [34] J. M. Ralston and R. K. Chang, "Spontaneous-Raman-scattering efficiency and stimulated scattering in silicon," *Phys. Rev. B, Condens. Matter*, vol. 2, no. 6, pp. 1858–1862, Sep. 1970.
- [35] T. R. Hart, R. L. Aggarwal, and B. Lax, "Temperature dependence of Raman scattering in silicon," *Phys. Rev. B, Condens. Matter*, vol. 1, no. 2, pp. 638–642, Jan. 1970.
- [36] P. A. Temple and C. E. Hathaway, "Multiphonon Raman spectrum of silicon," *Phys. Rev. B, Condens. Matter*, vol. 7, no. 8, pp. 3685–3697, Apr. 1973.
- [37] R. Claps, D. Dimitropoulos, Y. Han, and B. Jalali, "Observation of Raman emission in silicon waveguides at 1.54 μm ," *Opt. Express*, vol. 10, no. 22, pp. 1305–1313, Nov. 2002.
- [38] R. Claps, D. Dimitropoulos, V. Raghunathan, Y. Han, and B. Jalali, "Observation of stimulated Raman amplification in silicon waveguides," *Opt. Express*, vol. 11, no. 15, pp. 1731–1739, Jul. 2003.
- [39] T. K. Liang and H. K. Tsang, "Role of free carriers from two-photon absorption in Raman amplification in silicon-on-insulator waveguides," *Appl. Phys. Lett.*, vol. 84, no. 15, pp. 2745–2747, Apr. 2004.
- [40] R. L. Espinola, J. I. Dadap, R. M. Osgood, Jr., S. J. McNab, and Y. Vlasov, "Raman amplification in ultrasmall silicon-on-insulator waveguides," *Opt. Express*, vol. 12, no. 16, pp. 3713–3718, Aug. 2004.
- [41] H. Rong, A. Liu, R. Nicolaescu, M. Paniccia, O. Cohen, and D. Hak, "Raman gain and nonlinear optical absorption measurement in a low loss silicon waveguide," *Appl. Phys. Lett.*, vol. 85, no. 12, pp. 2196–2198, Sep. 2004.
- [42] A. Liu, H. Rong, M. Paniccia, O. Cohen, and D. Hak, "Net optical gain in a low loss silicon-on-insulator waveguide by stimulated Raman scattering," *Opt. Express*, vol. 12, no. 18, pp. 4261–4267, Sep. 2004.
- [43] Q. Xu, V. Almeida, and M. Lipson, "Time-resolved study of Raman gain in highly confined silicon-on-insulator waveguides," *Opt. Express*, vol. 12, no. 19, pp. 4437–4442, Sep. 2004.
- [44] T. K. Liang and H. K. Tsang, "Efficient Raman amplification in silicon-on-insulator waveguides," *Appl. Phys. Lett.*, vol. 85, no. 16, pp. 3343–3356, Nov. 2004.
- [45] B. Jalali, V. Raghunathan, O. Boyraz, R. Claps, and D. Dimitropoulos, "Wavelength conversion and light amplification in silicon waveguides," in *Proc. Group IV Photonics Conf.*, Hong Kong, Sep. 29–Oct. 1, 2004, pp. 10–12.
- [46] O. Boyraz and B. Jalali, "Demonstration of a silicon Raman laser," *Opt. Express*, vol. 12, no. 21, pp. 5269–5273, Oct. 2004.
- [47] R. Jones, H. Rong, A. Liu, A. W. Fang, M. Paniccia, D. Hak, and O. Cohen, "Net continuous-wave optical gain in a low loss silicon-on-insulator waveguide by stimulated Raman scattering," *Opt. Express*, vol. 13, no. 2, pp. 519–525, Jan. 2005.
- [48] H. Rong, A. Liu, R. Jones, O. Cohen, D. Hak, R. Nicolaescu, A. Fang, and M. Paniccia, "An all-silicon Raman laser," *Nature*, vol. 433, no. 7023, pp. 292–294, Jan. 2005.

- [49] H. Rong, R. Jones, A. Liu, O. Cohen, D. Hak, A. Fang, and M. Paniccia, "A continuous-wave Raman silicon laser," *Nature*, vol. 433, no. 7027, pp. 725–728, Feb. 2005.
- [50] K. Mizoguchi and S. Nakashima, "Determination of crystallographic orientations in silicon films by Raman-microprobe polarization measurements," *J. Appl. Phys.*, vol. 65, no. 7, pp. 2583–2590, Apr. 1989.
- [51] R. A. Soref, J. Schmidtchen, and K. Petermann, "Large single-mode rib waveguides in GeSi-Si and Si-on-SiO₂," *IEEE J. Quantum Electron.*, vol. 27, no. 8, pp. 1971–1974, Aug. 1991.
- [52] S. Pogossian, L. Vescan, and A. Vonsovici, "The single mode condition for semiconductor rib waveguides with large cross-section," *J. Lightw. Technol.*, vol. 16, no. 10, pp. 1851–1853, Oct. 1998.
- [53] [Online]. Available: <http://www.photond.com>
- [54] A. Taflov and S. C. Hagness, *Computational Electrodynamics: The Finite-Difference Time-Domain Method*, 2nd ed. Boston, MA: Artech House, 2000.
- [55] H. K. Tsang, C. S. Wong, T. K. Liang, I. E. Day, S. W. Roberts, A. Harpin, J. Drake, and M. Asghari, "Optical dispersion, two photon absorption and self-phase modulation in silicon waveguides at 1.5 μm wavelength," *Appl. Phys. Lett.*, vol. 80, no. 3, pp. 416–418, Jan. 2002.
- [56] M. Dinu, F. Quochi, and H. Garcia, "Third-order nonlinearities in silicon telecom wavelengths," *Appl. Phys. Lett.*, vol. 82, no. 18, pp. 2954–2956, May 2003.
- [57] A. Villeneuve, C. C. Yang, G. I. Stegeman, C. N. Ironside, G. Scelsi, and R. M. Osgood, "Nonlinear absorption in a GaAs waveguide just above half the band gap," *IEEE J. Quantum Electron.*, vol. 30, no. 5, pp. 1172–1174, May 1994.
- [58] D. V. Thourhout, C. R. Doerr, C. H. Joyner, and J. L. Pleumeekers, "Observation of WDM crosstalk in passive semiconductor waveguides," *IEEE Photon. Technol. Lett.*, vol. 13, no. 5, pp. 457–459, May 2001.
- [59] R. A. Soref and P. J. Lorenzo, "All-silicon active and passive guided-wave components for $\lambda = 1.3$ and $1.6 \mu\text{m}$," *IEEE J. Quantum Electron.*, vol. QE-22, no. 6, pp. 873–879, Jun. 1986.
- [60] [Online]. Available: www.silvaco.com
- [61] J. Auyeung and A. Yariv, "Theory of CW Raman oscillation in optical fibers," *J. Opt. Soc. Amer.*, vol. 69, no. 6, pp. 803–807, Jun. 1979.
- [62] G. Varella, O. Audouin, and E. Desurive, "Numerical optimization of power conversion efficiency in 1480 nm multi-Stokes Raman fiber lasers," *Electron. Lett.*, vol. 34, no. 7, pp. 675–676, Apr. 1998.
- [63] M. Rini, I. Cristiani, and V. Degiorgio, "Numerical modeling and optimization of cascaded CW Raman fiber lasers," *IEEE J. Quantum Electron.*, vol. 36, no. 10, pp. 1117–1122, Oct. 2000.
- [64] A. Liu, L. Liao, H. Rong, R. Jones, D. Samara-Rubio, D. Rubin, R. Cohen, O. Cohen, D. Hak, T. Franck, U. D. Keil, and M. Paniccia "Recent development in silicon photonics: 2.5 Gb/s silicon optical modulator and silicon Raman laser," *Proc. SPIE*, Mar. 2005, vol. 5730, pp. 80–93.
- [65] M. Krause, H. Renner, and E. Brinkmeyer, "Analysis of Raman lasing characteristics in silicon-on-insulator waveguides," *Opt. Express*, vol. 12, no. 23, pp. 5703–5710, Nov. 2004.
- [66] E. Garmire, "Criteria for optical bistability in a lossy saturating Fabry-Pérot," *IEEE J. Quantum Electron.*, vol. 25, no. 3, pp. 289–295, Mar. 1989.
- [67] R. Jones, A. Liu, H. Rong, M. Paniccia, O. Cohen, and D. Hak, "Lossless optical modulation in a silicon waveguide using stimulated Raman scattering," *Opt. Express*, vol. 13, no. 5, pp. 1716–1723, Mar. 2005.
- [68] V. Raghunathan, R. Claps, D. Dimitropoulos, and B. Jalali, "Wavelength conversion in silicon using Raman induced four-wave-mixing," *Appl. Phys. Lett.*, vol. 85, no. 1, pp. 34–36, Jul. 2004.
- [69] R. K. Jain, C. Lin, R. H. Stolen, and A. Ashkin, "A tunable multiple Stokes CW fiber Raman oscillator," *Appl. Phys. Lett.*, vol. 31, no. 2, pp. 89–90, Jul. 1977.
- [70] D. I. Chang, H. K. Lee, and K. H. Kim, "Cascaded Raman fibre laser operating at 1.48 μm ," *Electron. Lett.*, vol. 35, no. 22, pp. 1951–1952, Oct. 1999.

Ansheng Liu received the Ph.D. degree in physics from the University of Aalborg, Aalborg, Denmark, in 1992.

He is currently a Research Scientist and Senior Staff Member with the Photonic Technology Laboratory, Intel Corporation, Santa Clara, CA, where he is developing silicon photonic devices in the Corporate Technology Group. Before joining Intel in 2000, he worked at NASA Ames Research Center, Moffett Field, CA; the National Institute of Standards and Technology, Gaithersburg, MD; and at the University of Aalborg as an Assistant Professor. His interests include nonlinear optics of nanostructures, near-field optics, opto-electronics, and photonics. He has authored or co-authored more than 80 publications in these fields and contributed to 40 patents.

Haisheng Rong received the Ph.D. degree in physics from the University of Heidelberg, Germany, in 1992 and the B.S. and M.S. degrees in optics from Nankai University, Nankai, China, in 1983 and 1986, respectively.

He is a senior scientist in the Photonics Technology Lab, Intel's Corporate Technology Group, Santa Clara, CA. He is currently leading the Raman silicon laser research project and studying nonlinear optical effects in silicon waveguide-based photonics devices. He has worked in many areas of optical and laser technologies during his career, including high-resolution laser spectroscopy, laser interferometer gravitational-wave detection, and optical communications and interconnects.

Richard Jones received the B.Sc. and Ph.D. degrees in physics from Imperial College, London University, London, U.K., in 1993 and 1998, respectively, and the M.Sc. degree in microwaves and optoelectronics from University College, London University, in 1994.

He has been working as a Senior Optical Researcher in the Photonic Technology Laboratory, Intel Corp., Santa Clara, CA, since 2001. His research interests in silicon photonics include nonlinear optics, active optical components for communication systems, and optical sensing.

Dr. Jones is a member of the Optical Society of America (OSA) and the American Chemical Society (ACS).

Oded Cohen received the M.Sc. degree in solid-state experimental physics in 1993 and the B.Sc. in mathematics and physics in 1990, both from the Hebrew University, Jerusalem, Israel.

He is currently a senior process development engineer for the Silicon Photonics processing group at Intel, Jerusalem. He has 12 years experience at Intel on various engineering groups involved in CMOS and Flash memory process development of deep UV photolithography, RIE etching, thin-film PECVD, and thin-film metrology. His research interests include integrated optoelectronics, silicon photonics, and waveguide Bragg gratings.

Dani Hak was born in Israel in 1975. He received the B.Sc. degree in computer sciences and physics from the Hebrew University, Jerusalem, Israel, in 2003. From 2002 to 2005, he worked for Intel Corporation, Jerusalem, in process development of Silicon photonics devices. Currently, he is pursuing the M.Sc. degree at Tel-Aviv University, Tel-Aviv, Israel.

His current research interests include waveguide-based detectors.

Mario Paniccia (SM'04) received the B.S. degree in physics in 1988 from the State University of New York, Binghamton, and the Ph.D. degree in solid-state physics from Purdue University, West Lafayette, IN, in 1994.

He is Senior Principal Engineer and Director of Intel's Photonics Technology Lab, Santa Clara, CA. He has worked in many areas of optical technologies during his career, including optical testing for leading edge microprocessors, optical communications, and optical interconnects.